


Magnetic Microbubbles Combined with ICG-Loaded Liposomes for Synergistic Mild-Photothermal and Ferroptosis-Enhanced Photodynamic Therapy of Melanoma

Kaifen Xiong^{1,2}, Guanghong Luo³, Wei Zeng⁴, Guanxi Wen⁴, Chong Wang^{1,5,6}, Aijia Ding^{1,2}, Min Qi⁷, Yingying Liu⁴, Jianglin Zhang^{1,5,6} 

¹Department of Dermatology, Shenzhen People's Hospital, The second Clinical Medical College, Jinan University; The First Affiliated Hospital, Southern University of Science and Technology, Shenzhen, Guangdong, People's Republic of China; ²Department of Dermatology, Xiangya Hospital, Central South University, Changsha, Hunan, People's Republic of China; ³Department of Radiation Oncology, Shenzhen People's Hospital, The second Clinical Medical College, Jinan University; The First Affiliated Hospital, Southern University of Science and Technology, Shenzhen, Guangdong, People's Republic of China; ⁴Department of Ultrasonography, Shenzhen People's Hospital, second Clinical Medical College of Jinan University, First Clinical Medical College of Southern University of Science and Technology, Shenzhen, Guangdong, People's Republic of China; ⁵Candidate Branch of National Clinical Research Center for Skin Diseases, Shenzhen, Guangdong, People's Republic of China; ⁶Department of Geriatrics, Shenzhen People's Hospital, The second Clinical Medical College, Jinan University; The First Affiliated Hospital, Southern University of Science and Technology, Shenzhen, Guangdong, People's Republic of China; ⁷Department of Plastic Surgery, Shenzhen Hospital, Southern Medical University, Shenzhen, People's Republic of China

Correspondence: Yingying Liu; Jianglin Zhang, Email yingyingliu@ext.jnu.edu.cn; zhang.jianglin@szhospital.com

Background: Melanoma poses a significant threat to human health due to the lack of effective treatment options. Previous studies have demonstrated that the combination of photothermal therapy (PTT) and photodynamic therapy (PDT) can enhance therapeutic efficacy. However, conventional PTT/PDT combination strategies face various challenges, including complex preparation processes, potential damage to healthy tissues, and insufficient generation of reactive oxygen species (ROS). This study aims to design a rational and efficient PTT/PDT therapeutic strategy for melanoma and to explore its underlying mechanisms.

Methods: We first synthesized two target materials, indocyanine green-targeted liposomes (ICG-Lips) and magnetic microbubbles (MMBs), using the thin-film hydration method, followed by characterization and performance evaluation of both materials. Subsequently, we evaluated the synergistic therapeutic effects and underlying mechanisms of ICG-Lips combined with MMBs in melanoma treatment through in vitro experiments using cellular models and in vivo experiments using animal models.

Results: Herein, we developed a multifunctional system comprising ICG-Lips and MMBs. ICG-Lips enhance targeted delivery through specific binding to the S100B protein on melanoma cells, while MMBs, via ultrasound (US)-induced cavitation effects, shorten the uptake time of ICG-Lips by melanoma cells and improve uptake efficiency. Furthermore, the combination of ICG-Lips and MMBs induces significant reactive oxygen species (ROS) generation. Under 808 nm laser irradiation, the accumulation of ICG-Lips in melanoma cells achieves mild photothermal therapy (mPTT) and PDT effects. The elevated temperature and excessive ROS generated during these processes result in glutathione (GSH) depletion, ultimately triggering ferroptosis. The occurrence of ferroptosis further amplifies PDT efficacy, creating a synergistic effect that effectively suppresses melanoma growth. Additionally, the combined therapeutic strategy of ICG-Lips and MMBs demonstrates excellent biosafety.

Conclusion: In summary, this study presents a novel and straightforward strategy that integrates mPTT, PDT, and ferroptosis synergistically to combat melanoma, thereby laying a solid foundation for improving melanoma treatment outcomes.

Keywords: magnetic microbubbles, ferroptosis, mild-temperature photothermal therapy, photodynamic therapy, synergistic therapy

Introduction

Melanoma is a highly malignant skin cancer that poses a severe threat to global human health, with a high incidence and mortality rate among skin cancers.^{1,2} Due to the inherently aggressive nature of melanoma, traditional treatment methods such as surgical intervention, chemotherapy, and radiation therapy have limited efficacy in improving patient prognosis.³ Recently, the exploration of immunotherapy, including immune checkpoint inhibitors (ICIs), chimeric antigen receptor T-cell (CAR-T) therapy, and vaccines, has shown significant improvement in prognosis, especially for patients with metastatic melanoma.^{4,5} However, due to factors such as the high heterogeneity of melanoma, the overall response rate to immunotherapy remains low. The therapeutic effects of existing treatments fall far short of expectations. In this context, many researchers are dedicated to elucidating key molecular mechanisms and developing new diagnostic and therapeutic strategies, with the aim of discovering novel treatment approaches for melanoma.^{6–8}

In the past decades, the superiority of nanoparticles in delivering therapeutic agents to tumor cells, reducing drug toxicity, and facilitating synergistic therapy has been widely recognized, which promotes a big step forward in medicine and proposes many innovative therapeutic modalities such as Photothermal therapy (PTT), photodynamic therapy (PDT), Chemodynamic therapy (CDT), and sonodynamic therapy (SDT), etc.^{9–11} Among the therapeutic modalities, PTT and PDT are particularly noteworthy because of their excellent temporal and spatial controllability, low toxicity, and noninvasiveness.^{12,13} PTT involves the absorption of light energy by photothermal agents (PTAs), which convert light into heat energy to increase local hyperthermia and effectively kill cancer cells effectively.¹⁴ Three primary target temperature ranges were classified: 1. Tumor cell cytoclast ablative therapies ($>50^{\circ}\text{C}$) that induce coagulative necrosis; 2. High-temperature focal hyperthermia ($>43^{\circ}\text{C}$) leads to irreversible cellular damage, delayed cellular damage, ischemia, and inflammatory infiltration; 3. Moderate hyperthermia (mPTT) ($38\text{--}43^{\circ}\text{C}$ / $42\text{--}45^{\circ}\text{C}$), which enhances tumor immunogenicity by inducing sublethal cellular damage and increasing immune cell tumor transit.^{15,16} All three temperatures used in the treatment effectively killed the cancer cells. For example, Pandesh et al synthesized a nanomaterial composite consisting of Fe_3O_4 and gold owing to its excellent photothermal conversion efficiency (PCE), which can inhibit the growth of mouse melanoma under magnetically targeted selective PTT.¹⁷ Clinically, PTT involves the induction of local temperature elevation at moderate temperatures owing to the relatively high sensitivity of malignant cells to hyperthermia, which leads to apoptosis/necrosis of tumor cells to facilitate oncological therapies. Disappointedly, when the temperature of the PPT exceeds 45°C , it may cause thermal damage to healthy tissues surrounding the tumor and tumors often persist and subsequently recur when treated with PTT monotherapy because of the limited tissue penetration of NIR.^{18,19} Therefore, mild-temperature PTT (mPTT) or its combination with other treatment modalities is generally considered the optimal choice. mPTT induces thermal damage or apoptosis in tumor cells by locally generating heat. It not only kills tumor cells directly through the thermal effect but also enhances the anti-tumor response by activating immune reactions and promoting changes in the tumor microenvironment. For instance, mPTT can increase immune cell infiltration in tumor regions and activate specific immune responses.²⁰

In PDT, photosensitizers (PS) are excited by NIR, transferring energy to the surrounding oxygen molecules and generating reactive oxygen species (ROS) (including hydroxyl radicals, superoxide anion radicals, singlet oxygen, and hydrogen peroxide radicals), which ROS causes excessive oxidative damage to cancer cells, leading to tumor cell death.²¹ Normally, PDT is classified into two types. Type I PDT involves the direct binding of substrates or molecules on the cell membrane, resulting in the transfer of an electron to form a free radical. Type II PDT converts oxygen molecules into active singlet oxygen via energy conversion.²² The balance between the two types of PDT varies depending on factors such as photosensitizer type, light conditions, tumor microenvironment, and tissue oxygen concentration.²³ Hypoxic conditions within the tumor microenvironment and tumor cells exhibit elevated levels of intracellular antioxidant glutathione (GSH) to fulfill their antioxidant function, which significantly limits PDT efficacy by hindering ROS generation.^{24–26} Therefore, strategies focused on disrupting the antioxidant function of tumor cells to stimulate ROS production represent a promising approach for enhancing anti-tumor efficacy. Theoretically, synergistic outcomes of PTT and PDT are expected.

In PTT and PDT, the nanomaterial applied is a key factor in nanomedicine. Among the different nanoparticles, ICG, a fluorescence imaging reagent, was approved for clinical use by the FDA as early as 1956, and has recently attracted

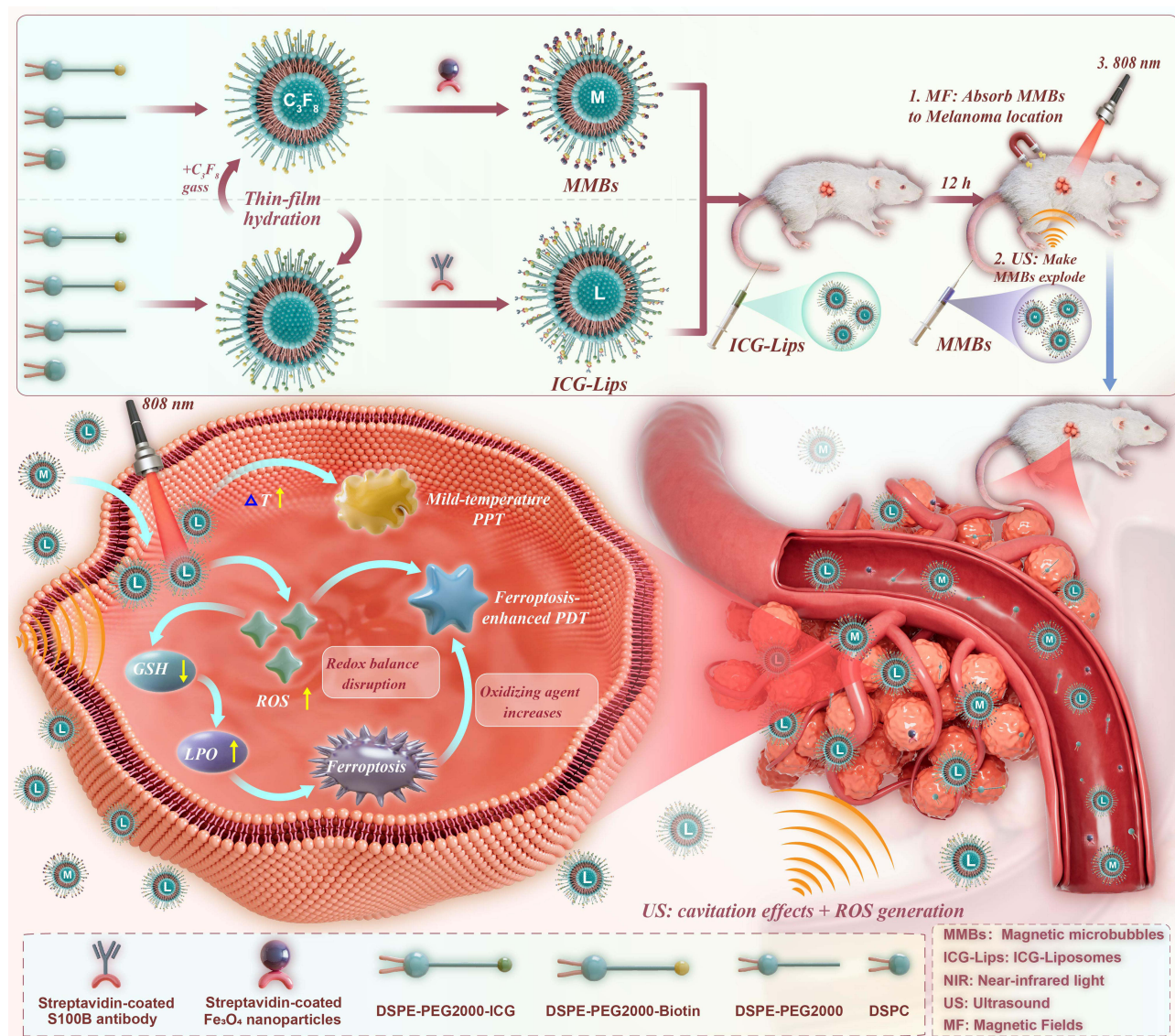
much interest in PTT and PDT. Previous research suggests that ICG can serve as a PTA and PS for PTT and PDT under approximately 800 nm laser irradiation to combat tumors simultaneously.^{27–29} Various ICG Nanoparticles have been used in therapeutic studies on melanoma.^{30,31} Meanwhile, ICG-based PDT have been proved to induce ferroptosis in fibrosarcoma cell lines by altering lipid ROS levels,³² but there is no evidence whether ICG could induce ferroptosis in melanoma. ICG has several limitations, including a short half-life (2–4 minutes), self-aggregation in physiological solutions, poor photostability and hydrolytic stability, nonspecific binding to proteins, and lack of specific targeting, which hinder its accumulation and therapeutic efficacy in medical applications. As a result, various carriers have been explored for ICG delivery. Liposomes are considered the preferred drug delivery vehicles, particularly for mRNA-based vaccines. For instance, EphA2-targeted nanotherapeutics and aerosolized mRNA have been developed and applied in pulmonary treatments.^{33,34} In this study, liposomes were also introduced as a delivery vehicle for ICG. However, liposomes lack active targeting capabilities, limiting their therapeutic efficacy, which has spurred the development of various enhancement strategies. One such approach involves the cavitation effect of ultrasound (US)-induced microbubbles (MBs), which significantly improves the delivery efficiency of nanomedicines. MBs are a commonly used US contrast agent in clinical practice. Mediated by US, the vibration and expansion of MBs in liquids to the point of rapid collapse and destruction is known as the cavitation effect, and this process generates shock waves, which facilitate the entrance of drugs or sensitizers, etc., into the cells by improving the permeability of the cell membrane. In addition, gas-filled MBs may cleave to produce an acoustic luminescence effect, generating ROS, and the rupture of MBs leading to localized temperature elevation also promotes the generation of ROS.^{35,36} It has been demonstrated that ultrasound-mediated MBs destruction inhibits melanoma growth in both cellular and animal models.^{37,38} Utilization of MBs for adjuvant cancer therapy has been clinically reported. For example, Dimcevski et al demonstrated that US combined with phospholipid MBs (SonoVues) dramatically improved the response to gemcitabine in patients with pancreatic ductal adenocarcinoma.³⁹ However, there are limitations of MBs such as low binding capacity, short retention time, and lack of specificity and sensitivity and conquering these limitations will have a favorable effect on their application.

Inspired by previous findings, this study introduced a stable and multifunctional system comprising ICG-Lips with targeting characteristics and magnetic microbubbles (MMBs) that exhibit both targeting and cavitation effects for synergistic treatment of melanoma using mPTT and ferroptosis-enhanced PDT. As illustrated in [Scheme 1](#), the ICG-Lips and MMBs were prepared via a thin-film hydration method. Using an external magnetic field, MMBs were directed to surround melanoma cells. Under ultrasound stimulation, MMBs induced a cavitation effect that facilitated the entry of ICG-Lips into melanoma cells and promoted ROS generation. Upon near-infrared irradiation, ICG-Lips experienced a temperature rise, triggering the mPTT effect, while simultaneously generating ROS to exert the PDT effect. The generation of ROS can lead to lipid metabolism dysregulation and GSH depletion, resulting in ferroptosis in melanoma cells. The oxidative stress and accumulation of lipid peroxides associated with ferroptosis increase cellular vulnerability, potentially making the cells more sensitive to PDT. Overall, both in vitro and in vivo results demonstrated that ICG-Lips combined with MMB-activated PTT/ferroptosis-enhanced PDT exhibited a synergistic effect with high biological safety. This study provides a safe and effective therapeutic strategy for melanoma.

Materials and Methods

Materials

Indocyanine Green (ICG 95%), streptavidin-coated superparamagnetic Fe₃O₄ NPs (5 mg/mL, ~130 nm), and 1,2-distearoyl-sn-glycero-3-phosphoethanolamine-N- [Indocyanine Green (polyethylene glycol)-2000] (DSPE-PEG₂₀₀₀-ICG) were purchased from Haoran Biotechnology Co. Ltd. (Xi'an, China). 1,2-distearoyl-sn-glycero-3-phosphoethanolamine-N- [biotinyl (polyethylene glycol)-2000] (DSPE-PEG₂₀₀₀-biotin) was obtained from Ruixi Biological Technology Co., Ltd. (Xi'an, China). 1,2-distearoyl-sn-glycero-3-phosphoethanolamine-N- [methoxy (polyethylene glycol)-2000] (DSPE-PEG₂₀₀₀) and 1,2-distearoyl-sn-glycero-3-phosphocholine (DSPC) were purchased from Avanti Polar Lipids (Alabaster, USA). The streptavidinylated S100B-antibody was purchased from the Cloud-Clone Corporation (Wuhan, China). Dialysis bags (MW:8–14kDa), Calcein-AM/ Propidium Iodide (PI) Cell Cytotoxicity assay kits, Cell Counting Kit-8 (CCK-8), and Hoechst 33342 were obtained from Solarbio Science & Technology Co., Ltd. (Beijing,



Scheme 1 Synthesis route of ICG-Lips, MMBs, and the mechanism of their synergistic action against melanoma.

China). Ferrostatin-1 (Fer-1, 99.89%), 9,10-anthracenediylbis (methylene) dimalonic acid (ABDA, $\geq 90\%$), and BODIPY^{581/591}-C11 probes were purchased from MedChemExpress (NJ, USA). CM-H2DCFDA and apoptosis Annexin V-FITC/PI kits were obtained from KeyGEN Biotech (Nanjing, China). All the chemicals and materials were used as received without further purification.

Preparation of ICG-Lips and MMBs

ICG-Lips and MMBs were prepared via thin-film hydration. Briefly, DSPC, DSPE-PEG₂₀₀₀, DSPE-PEG₂₀₀₀-biotin, and DSPE-PEG₂₀₀₀-ICG were dissolved in a solvent mixture of 18 mL chloroform and 2 mL methanol at a molar ratio of 73:9:9:9. After stirring for 30 min, the solvent was evaporated by rotary evaporation for 2 h to generate a thin lipid layer. Subsequently, the film was dried in a vacuum chamber overnight, hydrated in PBS solution at 60 °C for 15 min, the liposomal suspension was sonicated for 2 min, and extruded by passing through 220 nm polycarbonate filters. Streptavidin-coated S100B antibody was added to the synthesized ICG-Lip solution for 15 min to obtain the targeted ICG-Lips. Finally, dialysis (molecular weight cutoff = 8–12 kDa) at 4 °C was conducted for 24 h to remove non-

encapsulated ICG and free streptavidin-encapsulated superparamagnetic S100B antibody. Blank liposomes and non-targeted ICG-Lips were prepared under similar conditions following the same procedure.

MMBs were prepared using a procedure similar to that used to prepare the ICG-Lips. Biotinylated microbubbles (BMBs) were synthesized as previously described.^{40,41} Subsequently, MMBs were fabricated by introducing streptavidin-coated Fe₃O₄ NPs into BMBs solution for 15 min.

Characterization

The morphology of the nanoparticles was observed via transmission electron microscopy (TEM, Tecnai G20, FEI Corp., USA) using the negative staining method. The morphology of MMBs was captured using an inverted fluorescence microscope (Leica DMi8, Germany). Particle size, polydispersity index (PDI), and zeta potential were determined using a ZetaSizer Nano series Nano-ZS (Malvern Instruments Ltd. Malvern, UK). FTIR analysis (in the wavelength range of 400–4000 cm⁻¹) was performed using FTIR (Perkin-Elmer Spectrum 100 FTIR) (VERTEK 80 v, Bruker, Billerica, MA, USA) to demonstrate the presence of ICG and S100B antibody in ICG-Lips. The concentrations of the prepared MMBs were measured using an accuser (Particle Sizing Systems, PSS A7000AD, USA). UV-Vis and fluorescence spectra were recorded using a Tecan Spark multifunctional microplate reader (Switzerland).

Stability Analysis of ICG-Lips and MMBs

ICG-Lips and free ICG dispersed in PBS solution were placed at a relatively low temperature (4 °C), room temperature (25 °C), and simulated normal human body temperature (37 °C). The absorption spectra of ICG-Lips and free ICG under different storage conditions were measured every other day using a Tecan Spark multifunctional microplate reader for a total of 14 days. The absorption spectra of ICG-Lips and free ICG under different storage temperature conditions and times were analyzed to assess their stability. Similarly, the stability of the BMBs and MMBs was assessed by dispersing them in PBS and measuring their residual percentage, particle size, and potential upon preparation and after 20, 40, and 60 min of storage under ambient conditions.

mPTT Performance, Photostability and PDT Performance Analysis

Equal amounts of free ICG and ICG (80 µg/mL) were placed in a cuvette and irradiated with 808 nm laser irradiation (2 W/cm²), and the temperatures of the solutions were recorded using an infrared camera after 3 min of laser irradiation to demonstrate the performance of mPTT.

To compare the photostability of the targeted ICG-Lips and ICG, the samples were exposed to an 808 nm laser for 3 min, followed by natural cooling to room temperature without further NIR laser irradiation, and the irradiation and cooling were repeated for five cycles.

For PDT evaluation, ABDA was used as an indicator (ICG-Lips: 80 µg/mL, ABDA: 2 mM) to analyze ROS generation. Briefly, ICG-Lips and ICG were suspended in a solution containing ABDA and irradiated with an 808 nm laser at a power of 2 W/cm², and the UV-Vis spectra of ABDA were recorded before and after NIR irradiation using a Tecan Spark multifunctional microplate reader.

Cell Culture

A375 were obtained from the American Type Culture Collection (Manassas, VA, USA) and were cultured in DMEM medium supplemented with FBS (10%), penicillin (1%, 50 U/mL), and streptomycin (1%, 50 U/mL) in a sterile incubator in a 5% CO₂ atmosphere (37 °C).

Cellular Uptake

A375 cells were inoculated in 6-well plates for 24 h and treated with six different treatments: free ICG, ICG-Lips, ICG-Lips + US, ICG-Lips + laser, ICG-Lips + MMBs, and ICG-Lips + MMBs + US. Following incubation at 37 °C for 5 min, 1 h, and 4 h, nuclei were stained with Hoechst33342 (λ_{ex} : 350 nm, λ_{em} : 440–460 nm) for 30 min. Subsequently, the cells were washed three times with PBS and imaged using a fluorescence microscope. Finally, the fluorescence of

ICG at different time points was quantified using ImageJ software. The uptake of ICG-Lips by PIG1 cells was measured and quantified using the same approach.

ROS and (Lipid Peroxide) LPO Generation Detection in Cancer Cells

A375 cells were seeded in 12-well plates and incubated overnight. The medium was replaced with PBS or serum-free medium containing ICG, ICG-Lip, MMB, or ICG-Lip + MMB. Following US irradiation (1.5 W/cm^2 , 20%, 1 min) and/or NIR laser irradiation (808 nm, 1 W/cm^2 , 10 min), the cells were further incubated at 37°C for 24 h. Subsequently, CM-H2DACDA solution ($10 \mu\text{M}$) was introduced into the cell culture medium for 20 min. The cell nuclei were stained with Hoechst 33342 (λ_{ex} : 350 nm, λ_{em} : 440–460 nm). Finally, fluorescence images were obtained using CLSM and quantified using the ImageJ software. LPO was assessed using the BODIPY^{589/591}-C11 probe in a manner similar to that used for ROS detection. LPO quantification was performed in the same manner as ROS quantification.

Cytotoxicity Assay

Cytotoxic effects on A375 cells were assessed using the CCK-8 cell counting kit, Calcein AM/PI staining, and Annexin V-FITC/PI combined with flow cytometry. For the CCK-8 assay, A375 cells were seeded in 96-well plates at a density of 5000 cells/well overnight, and the medium was replaced with PBS or serum-free medium containing ICG, ICG-Lips, MMB, or ICG-Lips + MMB. A375 cells were then treated with or without US irradiation and with or without NIR laser irradiation. After the treatment, the incubation was continued for 24 h, and then the cell culture medium was removed and 100 μL mixture of 5 μL CCK-8 and 95 μL serum-free DMEM culture medium for 1 h, the absorbance at 450 nm were measured using Tecan Spark multifunctional microplate reader. Cell viability was calculated using the following formula:

$$\text{Cell viability (\%)} = (\text{OD}_{450_{\text{samples}}} - \text{OD}_{450_{\text{blank}}}) / (\text{OD}_{450_{\text{control}}} - \text{OD}_{450_{\text{blank}}}) \times 100\%.$$

For the live/dead cell staining assay, A375 cells were inoculated into 24-well plates and cultured overnight, then the same medium substitutes and the same treatments as in the CCK8 assay were performed. After treatment, the cells were stained with calcein-AM for 30 min to visualize live cells and with propidium iodide (PI) for 30 min to visualize dead or late apoptotic cells. After staining, the cells were washed thrice with PBS and imaged using an inverted fluorescence microscope.

An apoptosis assay was performed using flow cytometry. Briefly, A375 cells were inoculated into 24-well plates and cultured overnight, and the same medium substitutes and treatments as in the CCK8 assay were performed. Following treatment, the cells were stained with an Annexin V-FITC/PI kit according to the manufacturer's instructions and analyzed using a flow cytometer and FlowJo V10 software.

GSH Level Measurement

A375 cells (2×10^5 cells/well) were seeded into 24-well plates. After exposure to the different treatments for 24 h, the cells were collected and lysed with liquid nitrogen, and the supernatant was collected by centrifugation at $8000 \times g$ for 10 min. The supernatants were tested using a GSH kit and the absorbance was measured at 412 nm using a Tecan Spark multifunctional microplate reader. Finally, the relative GSH levels were calculated according to the manufacturer's instructions. Ferrostatin-1 (Fer-1, $1 \mu\text{M}$) was added to the cells to investigate the role of the ferroptosis inhibitors.

Western Blotting Analysis of Glutathione Peroxidase 4 (GPX4) Expression

A375 cells (5×10^6 cells/well) were seeded in 6-well plates. After exposure to different treatments for 24 h, whole protein was extracted from cells using RIPA lysis and extraction buffer (Thermo Fisher Scientific, USA) and 1% PMSF (Thermo Fisher Scientific, USA). The protein concentrations were determined using a BCA protein assay kit (Beyotime, China). Proteins from each sample were separated using 12.5% SDS-PAGE and transferred to PVDF membrane. After sealing with 5% skim milk, the membranes were incubated overnight at 4°C with specific primary anti-GPX4 antibody (1:1000, NOVUS, nbp2-75511, USA), anti-S100B antibody = (1:1000, Affinity, DF6116, USA), and anti-GAPDH antibody (1:3000, Affinity, AF7021, USA). After washing with PBS three times, the membrane was incubated with

a horseradish peroxidase-coupled secondary antibody at room temperature for 1 h. Protein bands were visualized using electrochemiluminescence (Invitrogen) and the signal intensity of the bands was analyzed using ImageJ.

Untargeted Metabolomics Analysis

A375 cells treated under different conditions (control, MMBs+ICG-Lips+US+Laser) were used for the metabolomic analysis. The metabolites in the samples (three biological replicates per group) were extracted and dissolved in acetonitrile: H₂O (1:1 v/v). This solution was injected into the UPLC-MS/MS system for the analysis. Raw instrument data were exported to Compound Discoverer 3.1 (CD3.1). Identification of compounds using mzCloud (ddMS2) and ChemSpider (formula or accurate mass). Similarity searches were performed for all compounds with ddMS2 data using the mzCloud. Apply the mzLogic algorithm to sort ChemSpider results. Metabolomics was used to map the compounds to biological pathways. The QC samples were used for batch normalization. Differential analysis (*t*-test or ANOVA) was performed to determine p-values, adjusted p-values, ratios, fold changes, and CVs. Metabolites with P values < 0.05, FC < 0.67 or FC > 1.5 were considered as differential metabolites. Pathway analysis was performed using MetaboAnalyst 5.0.

Animals and A375 Xenograft Tumor Model

Female 4-week-old nude mice were purchased from Zhuhai BesTest Bio-Tech Co., Ltd. (Zhuhai, Guangdong, China). All animal experiments were approved by the Institutional Animal Care and Use Committee (IACUC) of the Experimental Animal Center of Shenzhen People's Hospital (Approval No. AUP-220226-ZJL-0001-01) and were conducted in strict accordance with the Guide for the Care and Use of Laboratory Animals and the relevant regulations of the Regulations for the Administration of Laboratory Animals of the People's Republic of China, to ensure the welfare of the experimental animals. A375 cells were collected and inoculated subcutaneously into the hind legs of anesthetized mice at a density of 5×10^6 cells/ mouse. The tumor volume was calculated as $1/2 \times (\text{length}) \times (\text{width}^2)$.

Biodistribution Analysis

A375 hormonal mice were intravenously injected with ICG (5 mg/kg), ICG-Lips (5 mg/kg), or MMBs (10^6 /mL), and their distribution at the tumor site at different time points was monitored using an IVIS imaging system (PerkinElmer, Waltham, MA, USA). After 48 h of drug administration, the mice were euthanized, and the major organs (heart, liver, spleen, lungs, and kidneys) and tumors were harvested and imaged ex vivo using an IVIS imaging system (PerkinElmer, Waltham, MA, USA).

In vivo Anti-Tumor Evaluation and Biosafety Evaluation

BALB/c nude mice were subcutaneously injected with A375 cells (5×10^6 cells/mouse), and when the tumor volume reached approximately 100 mm³, the mice were randomly divided into eight groups to receive different treatments, with four mice in each group: PBS (control), free ICG + US + laser, MMBs + US + laser, ICG-Lips + US + laser, ICG-Lips + MMBs + US, ICG-Lips + MMBs + laser, ICG-Lips + MMBs + US + laser (synergistic treatment group), and ICG-Lips + MMBs + US + laser + Fer-1. Tumor size and weight were monitored every other day for 14 days. At the end of the treatment period, the mice were euthanized, and the tumors were collected, photographed, and weighed. Tumor tissues were fixed and sliced for hematoxylin-eosin (HE) staining and immunohistochemical analysis of Ki67 and GPX4.

To assess the biosafety of the nanoparticles in vivo, the major organs (heart, liver, spleen, lung, and kidney) were extracted and analyzed by hematoxylin and eosin stain (H&E) staining. Routine blood and blood chemistry analyses included alanine aminotransferase (ALT), aspartate aminotransferase (AST), blood urea nitrogen (BUN), creatinine (CR), and uric acid (UA).

Statistical Analysis

The experimental data are expressed as mean \pm SD of at least three independent experiments. Comparisons of the experimental data between the two groups were performed using unpaired t-tests. Statistical analysis involved comparing the means across multiple groups using either one-way or two-way ANOVA, followed by post hoc Tukey's paired

comparisons. GraphPad Prism 9.0.0 was utilized for all statistical analyses. A probability value of $p < 0.05$ was considered statistically significant and statistical significance is defined as $*p < 0.05$, $**p < 0.01$, and $***p < 0.001$.

Results and Discussion

Synthesis and Characterization of ICG-Lips and MMBs

Both the ICG-lips and MMBs in our study were synthesized using the thin-film hydration method. Transmission electron microscopy (TEM) images of blank liposomes and ICG-Lips (Figure 1A left and right) both showed a distinct and typical spherical lipid morphology, indicating their stability in aqueous solutions. As indicated by the red arrows in Figure 1A, a black flocculent shadow is observed on the outer layer of ICG-Lips, while no such shadow is present in blank liposomes. This observation may suggest that the S100B antibody has been successfully loaded onto the surface of ICG-Lips. ICG-Lips were surrounded by matter on their surfaces compared to the blank liposomes. Furthermore, dynamic light scattering (DLS) analysis (Figure 1B) demonstrated that the size of ICG-Lips was approximately 180 ± 2.2 nm, consistent with the TEM observation. The particle size distribution of ICG-Lips exhibits enhanced permeability and retention (EPR) effects, making them suitable for passive targeted drug delivery.⁴² The average hydrodynamic diameters, PDI values, and zeta potentials of the ICG lips obtained by DLS are summarized in Table S1. The UV-visible absorption spectra (Figure 1C) revealed the characteristic absorption peak of free ICG at 779 nm, whereas the blank liposomes did

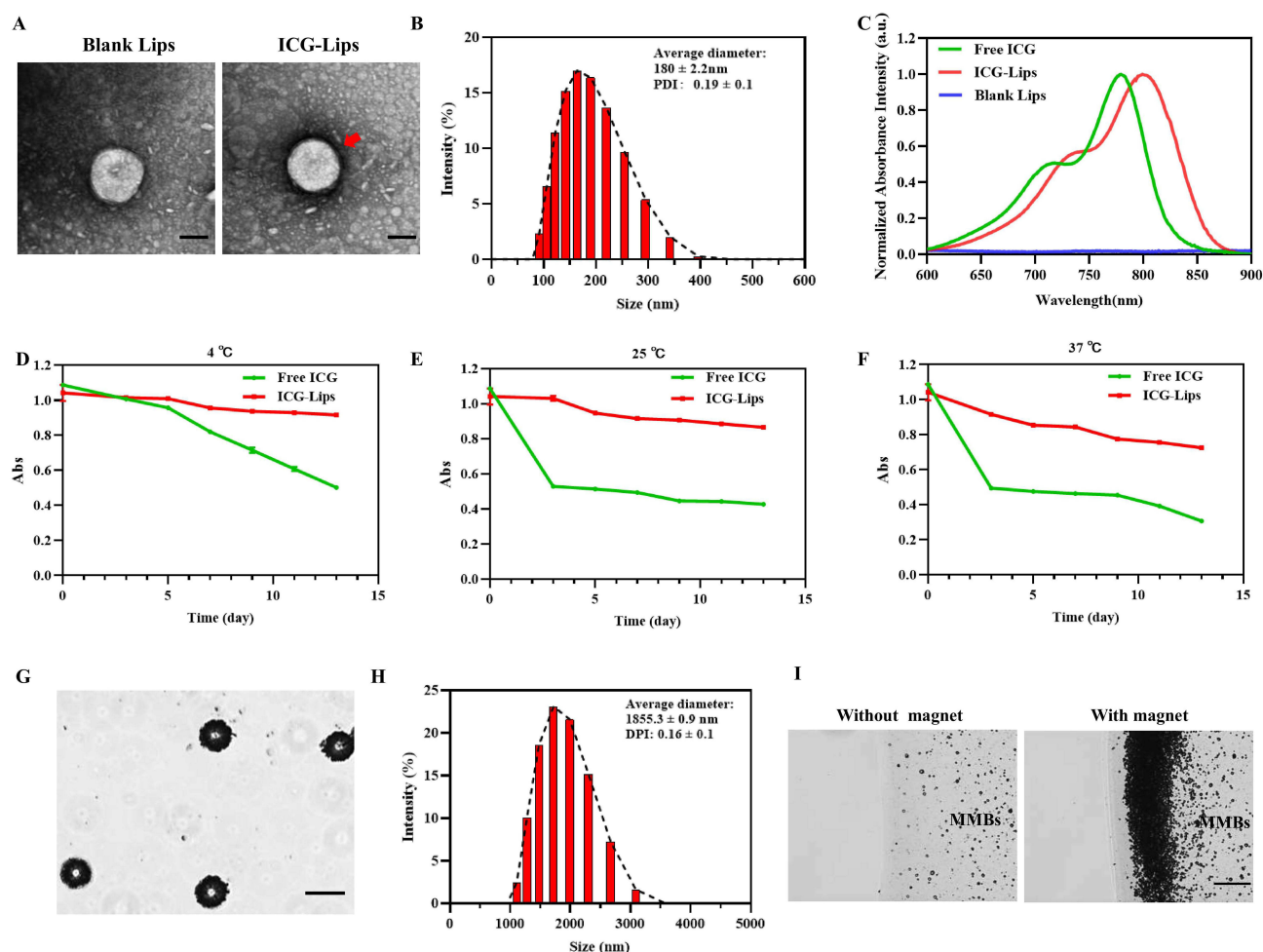


Figure 1 (A) TEM image of blank liposomes and ICG-Lips. The red arrows indicate the differences in the outer layer between ICG-Lips and blank liposomes. Scale bar: 100 nm. (B) The size distribution of ICG-Lips. (C) UV-vis absorption spectra of free ICG, blank liposomes, and ICG-Lips. (D-F) The absorption intensity variations of free ICG and ICG-Lips. (G) Typical optical microscope image of MMBs. Scale bar: 2 μ m. (H) The size distribution of MMBs. (I) Typical optical microscope images of MMBs in the absence and presence of a magnet. Scale bar: 200 μ m.

not display this peak. ICG-Lips exhibited a characteristic curve similar to that of free ICG, indicating successful loading of ICG within the liposomes. Notably, the encapsulation of ICG into lipids resulted in a 20 nm red-shifted absorbance that was slightly stronger than that of free ICG. This shift could be attributed to the hydrophobic nature of amphiphilic ICG molecules within the lipid bilayer of ICG-Lips.⁴³ The fluorescence spectrum of ICG-Lips is similar to that of free ICG, while blank liposomes exhibit no fluorescence spectrum, further confirming the successful synthesis of ICG-Lips without altering the inherent chemical properties of ICG^{44,45} (Figure S1A). Finally, Fourier-transform infrared spectroscopy (FTIR) was employed to confirm the successful loading of ICG and streptavidin-conjugated S100B antibody onto ICG-Lips. As shown in Figure S1B, the FTIR spectrum of ICG-Lips exhibited several characteristic peaks. Peaks at 665 cm^{-1} , 975 cm^{-1} , and 1420 cm^{-1} were attributed to the out-of-plane bending of C-H, vinyl stretching of C-H, and aromatic C=C stretching in ICG, respectively, indicating the incorporation of ICG into ICG-Lips.^{46,47} The C-H stretching vibration in the range of 2800–3000 cm^{-1} and the C-N stretching vibration at 1000–1100 cm^{-1} were clearly observed in both blank liposomes and ICG-Lips.⁴⁸ Additionally, the characteristic C-N stretching vibration peak at 1000–1200 cm^{-1} from the streptavidin-conjugated S100B antibody was also observed in ICG-Lips.^{49,50} Overall, these results confirm the successful preparation of ICG-Lips.

Although ICG has demonstrated efficacy as a fluorescent dye in bioimaging, its poor hydrolytic stability limits its broader applications.⁵¹ In this study, we aimed to assess whether the prepared ICG-Lips could enhance the hydrolytic stability of ICG, we evaluated the stability of ICG-Lips over 2 weeks at different storage temperatures (4, 25, and 35 °C) and time intervals (0, 1, 3, 5, 7, 9, 11 and 13 days) and the absorbance of both ICG-Lips and free ICG solutions, with equivalent ICG concentrations, was monitored to test their stability. As shown in Figure 1D-F, the absorbance values of free ICG at 4 °C, 25 °C, and 35 °C was decreased to 55%, 39%, and 36%, respectively, all of which showed significant decreases. Free ICG showed a lower decrease in absorbance during storage at low temperature (4 °C) than at room temperature (25 °C) and body temperature (37 °C), suggesting the high temperature benefits for ICG degradation. Conversely, the ICG-Lips exhibited a smaller decrease in absorbance at all three storage temperatures. The final absorbance levels were 88%, 83%, and 70% for storage temperatures of 4 °C, 25 °C, and 35 °C, respectively. Furthermore, the characteristic absorption curve of free ICG disappeared after 2 weeks of storage at various temperatures. In contrast, the synthesized ICG-Lips maintained characteristic curves similar to ICG even after 2 weeks of storage at 37 °C (Figure S1C-E). These results suggest that the hydrolytic stability of ICG was significantly improved in ICG-Lips. This may be attributed to the fact that ICG molecules condense in liposomes, avoiding direct contact with surrounding water.

Following our previous report,⁵² BMBs were fabricated via thin-film hydration, whereas MMBs were generated by conjugating streptavidin-labeled Fe_3O_4 (magnetic beads). Optical microscopy revealed that the MMBs appeared as uniform spherical structures with the magnetic beads effectively adhering to the microbubbles (Figure 1G). As shown in Figure 1H and Table S1, the particle size distribution of MMBs was $1.86 \pm 0.9 \mu\text{m}$ and the zeta potential was $-16.4 \pm 0.2 \text{ mV}$. As depicted in Figure S2A (left) displays top layer formation in a PBS solution of varying colors, similar to our earlier findings.⁵³ Magnets were utilized to check the magnetic responsiveness to verify whether MMBs were successfully synthesized, as shown in the optical image in Figure S2A (right), no movement of the BMBs was observed when the magnet was placed near the microbubble cake layer. However, the MMBs accumulated on the side where the magnet was placed, confirming the successful synthesis of the MMBs. The successful synthesis of MMBs was further confirmed by the fact that MMBs were uniformly distributed in the absence of an external magnetic field (Figure 1I, left), and displayed a near-field-measured distribution in the presence of an external magnetic field (Figure 1I, right) under an optical microscope. The BMBs and MMBs can spontaneously decompose. To evaluate the stability of MMBs, the same concentrations of BMBs and MMBs were measured after storage in PBS at room temperature for 20, 40, and 60 min and compared with the initially prepared samples (Figure S2B). The percentage of retention of both BMBs and MMBs was above 80% after 60 min, indicating that the MMBs were as well stabilized as the BMBs. Furthermore, the particle size and zeta potential of MMBs were measured after various storage durations (Figure S2C and D). These results demonstrate the excellent stability of MMBs.

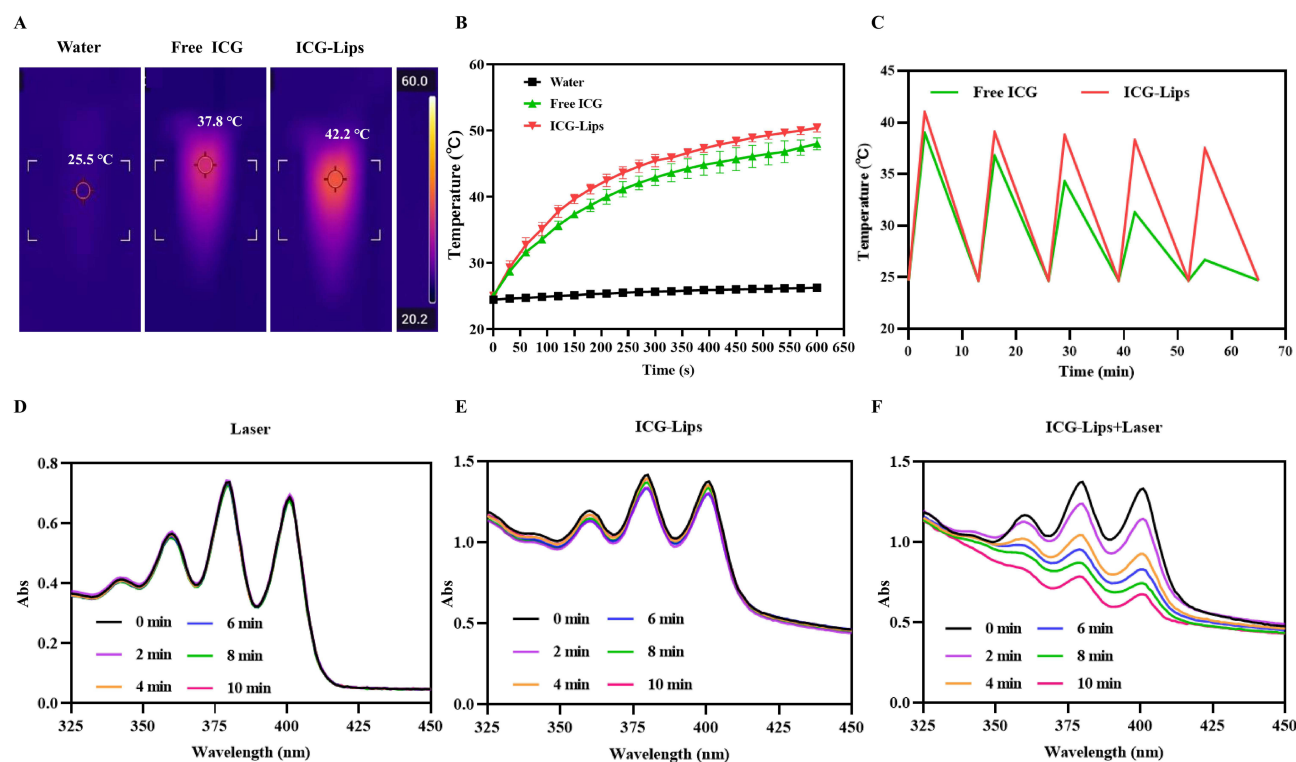


Figure 2 (A) The thermographic images of free Water, free ICG, and ICG-Lips in centrifuge tubes after laser irradiation. (808 nm, 2 W/cm², 3 min). (B) Temperature elevation of water, free ICG, and ICG-Lips at the same concentrations of ICG (80 µg/mL) with NIR laser irradiation (808 nm, 2.0 W/cm², 10 min). (C) Heating-cooling cycle curve of free ICG and ICG-Lips. (D) The spectrum of ABDA absorbance treated with pure laser irradiation for different times in the absence of ICG-Lips. (E) The spectrum of ABDA absorbance treated with ICG-Lips under room light for different times. (F) The spectra of ABDA absorbance treated with ICG-Lips upon different times of laser irradiation (808 nm, 2.0 W/cm², 10 min).

mPTT Effect and PDT Effect of ICG-Lips in vitro

To investigate the photothermal effect of ICG-Lips, the temperature elevation characteristics of aqueous solutions of free ICG and ICG-Lips, which contained the same concentration of ICG, upon NIR irradiation were examined (Figure 2A). Thermographic images (Figure 2B) indicated that the maximum temperatures reached by the ICG-Lips and free ICG were 37.8 °C and 42.2 °C, respectively. These results suggest that ICG-Lips have a promising potential for mPTT. Notably, the maximum temperature attained by ICG-Lips was higher than that of free ICG, possibly because of the stabilizing effect and altered absorption wavelength confined by liposomal encapsulation of ICG. Furthermore, the photothermal stability of both ICG-Lips and free ICG was investigated, and the temperature of the ICG-Lips solution increased to 41, 39.1, 38.8, 38.3, and 37.5 °C, while the temperature of the free ICG solution reached 39, 36.8, 34.3, 31.3, and 26.7 °C, respectively (Figure 2C). These findings indicated that ICG-Lips possessed better photothermal stability than free ICG. Figure S3A shows the dispersion coefficient of free ICG. Thereafter, different concentrations of ICG-Lips were irradiated to determine the appropriate concentration for mild-temperature PTT. As shown in Figure S3B, as the concentration of ICG-Lips increased, temperature-raising ability gradually increased. There was no statistically significant difference in temperature-raising ability when the concentration of ICG-Lips reached 80 µg/mL and 160 µg/mL. Therefore, we selected 80 µg/mL for subsequent studies.

To evaluate the PDT performance of ICG-Lips, we employed ABDA as a ROS indicator to evaluate the ability of ICG-Lip-based PDT in vitro.⁵⁴ As expected, there was no significant decrease in ABDA absorbance (350–425 nm) in ICG-Lips or laser-treated samples (Figure 2D and E), whereas in ICG-Lips-treated samples (Figure 2F), ABDA absorbance was significantly reduced after laser irradiation, suggesting that ICG-Lips have laser-dependent ROS generation ability.

Cellular Uptake and ROS Detection Study in vitro

To investigate the cellular uptake of free ICG and ICG-Lips under various conditions, the melanoma A375 cells were subjected to different treatments. Subsequently, the red fluorescence emitted by ICG and blue fluorescence emitted by the cell nuclei were captured at different time points using CLSM. Specifically, six groups were established: 1: free ICG; 2: ICG-Lips; 3: ICG-Lips + US; 4: ICG-Lips + laser; 5: ICG-Lips + MMBs, and 6: ICG-Lips + MMBs + US.

As shown in [Figure 3A](#) and [C](#), both the free ICG and ICG-Lips were predominantly distributed in the cytoplasm. At 5 min and 1 h after addition, the ICG fluorescence intensity in group 2 was not significantly different from that in group 1. However, at 4 h, the ICG fluorescence intensity in group 2 was notably stronger than that in group 1, which was attributed to the lipid bilayer structure of ICG-Lips that promoted cellular internalization owing to its superior stability.^{24,55} At 5 min, 1 h, and 4 h, there were no notable differences in ICG fluorescence intensity between Groups 3 and 5 when compared to Group 2, suggesting that ultrasound (US) irradiation alone and the presence of magnetic microbubbles (MMBs) alone did not influence the cellular uptake of ICG-Lips. The ICG fluorescence intensity of group 4 was comparable to that of group 2 at 5 min but was notably stronger at 1 and 4 h. This phenomenon may be attributed to noninvasive stimulation caused by photothermal energy and ROS generated through NIR irradiation, which alters membrane permeability and promotes cellular internalization.⁵⁶ Interestingly, the results showed a marked uptake of ICG-Lips in Group 6 at 5 min, which continued to increase at 1 and 4 h. The uptake efficiency in this group was significantly higher at each time point than that in the other groups, likely because of the cavitation effect of the MMB function. Overall, these results demonstrate that ICG-Lips exhibited superior A375 cell intake compared to free ICG. In addition, laser irradiation enhanced the uptake of ICG-Lips by A375 cells, whereas US irradiation in the presence of MMBs shortened the uptake time and enhanced the rate of uptake of ICG-Lips by A375 melanoma cells.

Previous studies have shown that ICGs possess PDT and SDT properties, whereas MMBs have SDT properties.^{57,58} Therefore, to examine whether different treatments could induce PDT and SDT in A375 cells, ROS generation in A375 cancer cells was detected in 15 groups; 1: US; 2, laser; 3, US + laser; 4, MMBs + US; 5, MMBs + laser; 6, MMBs + US + laser; 7, free ICG + US; 8, free ICG + laser; 9, free ICG + US + laser; 10, ICG-Lips + US; 11, ICG-Lips + laser; 12, ICG-Lips + US + laser; 13, ICG-Lips + MMBs + US; 14, ICG-Lips + MMBs + Laser; and 15, ICG-Lips + MMBs + US + laser. As shown in [Figure 3B](#) and [D](#), groups 1, 2, 3, 5, 7, and 10 exhibited no significant ROS generation. Groups 4, 6, and 10 showed only minimal ROS production, suggesting that microbubbles combined with US exhibited a slight SDT effect on A375 cells.^{58,59} Obvious ROS generation was observed in groups 8, 9, 11, 12, 14, and 15, which was attributed to the photodynamic properties of ICG.^{24,60} Notably, the most pronounced ROS generation was observed in Group 15, suggesting that the combination of MMBs and ICG-Lips could cause excessive ROS generation. Taken together, these findings suggest that ultrasound-mediated ROS production by MMBs is not significant, indicating that the SDT effect is less pronounced. However, under laser excitation, the ICG-Lips exhibited significant ROS generation, indicating good PDT efficacy. When ICG-Lips were combined with MMB, ROS generation was the most remarkable and the PDT effect was enhanced. Moreover, in a subsequent investigation ([Figure 5](#)), we observed significant alterations in ferroptosis-related markers with the combination of ICG-Lips and MMBs. Consequently, we hypothesized that the most pronounced ROS generation in this combined treatment group may be attributed to ferroptosis, which disrupts redox balance. Ferroptosis results in an increase in oxidants, thereby promoting ROS production, indicating a ferroptosis-enhanced PDT.

Anticancer Effects in vitro

Studies have shown that S100B protein expression is increased in melanoma.⁶¹ Our study also found that compared with normal melanocyte PIG1, S100B protein was highly expressed in melanoma A375 cells ([Figure S4A](#) and [B](#)). To enhance the ability of ICG-Lips to accumulate within tumors and address the inherent targeting deficiency of ICGs, the principle of antigen-antibody specific recognition was employed. This involved the conjugation of the S100B antibody to the prepared ICG-Lips for active targeting. As depicted in [Figure S5A-C](#), upon co-incubation of ICG-Lips with A375 melanoma cells for 4 h, laser confocal microscopy revealed that the fluorescence intensity was approximately three times greater than that observed with ICG-Lips co-incubated with normal melanocyte PIG1 cells for the same duration. Moreover, this fluorescence intensity was approximately four times higher than that observed for the ICG liposomes lacking the linked S100B

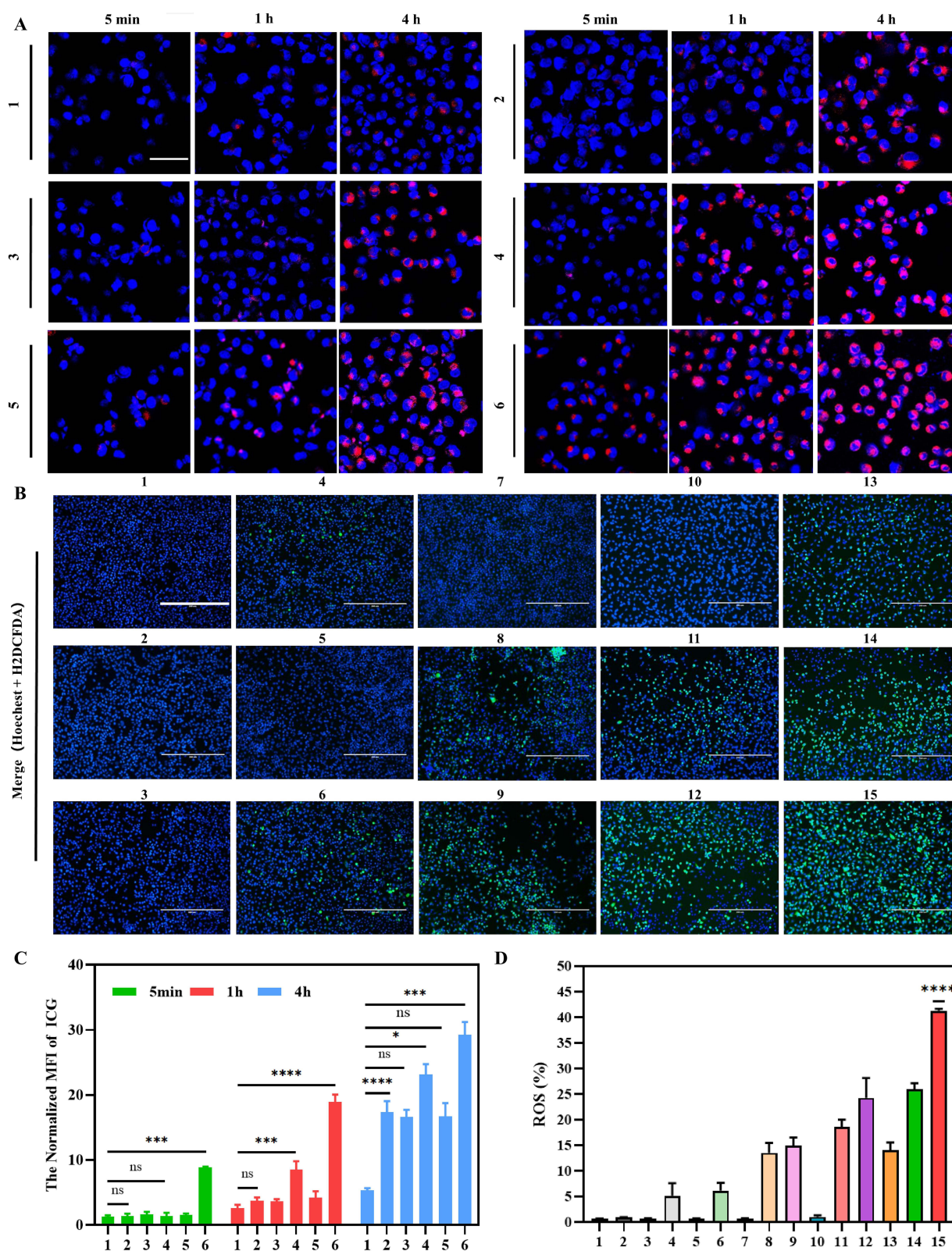


Figure 3 (A) Fluorescence images of A375 cells treated with different treatments at different time points. Scale bar: 50 μ m. The groups are set as: 1-free ICG; 2- ICG-Lips; 3-ICG-Lips + US; 4-ICG-Lips + laser; 5-ICG-Lips + MMBs; and 6-ICG-Lips + MMBs + US. (B) Fluorescence images of ROS generation in melanoma cell A375 following various treatments. Scale bar: 200 μ m. The groups are set as: 1-US; 2-laser; 3-US + laser; 4-MMBs + US; 5-MMBs + laser; 6-MMBs + US + laser; 7-free ICG +US; 8-free ICG + laser; 9-free ICG +US + laser; 10-ICG-Lips + US; 11-ICG-Lips + laser; 12-ICG-Lips + US + laser; 13-ICG-Lips + MMBs + US; 14-ICG-Lips + MMBs + Laser, and 15-ICG-Lips + MMBs + US+ laser. (C) is the quantification of (A). (D) is the quantification of (B). Free ICG and ICG-Lips at equal concentrations of ICG: 80 μ g/mL; US (1.5 W/cm², 20%, 1 min); Laser (808 nm, 1.0 W/cm², 10 min). n=3, ns: not significant ($p > 0.05$), * $p < 0.05$, *** $p < 0.001$, **** $p < 0.0001$, compared to the free ICG group/ the US group.

antibody. This demonstrates that ICG-Lips have a high target affinity for melanoma with an overexpression of S100B. To determine the optimal concentration of MMBs and the appropriate US conditions for subsequent experiments, the CCK-8 assay was used to assess the viability of A375 cells co-incubated with varying concentrations of MMBs or subjected to US irradiation at different intensities, times, and null ratios, depicted in [Figure S6A](#), at a concentration of 10^6 cells/mL and a US power of 1.5 W/cm^2 , the viability of A375 cells was above 85%, indicating suitable US conditions with minimal impact on cell viability. Moreover, alterations in the irradiation time and US duty cycle had no significant effects on A375 cell viability. Therefore, a standard US duration of 1 min and a duty cycle of 20% were selected ([Figure S6A](#)). Next, the CCK-8 assay was used to detect the viability of A375 cells co-incubated with MMBs and different concentrations of ICG-Lips and treated with US combination laser irradiation. As shown in [Figure S6B](#), cell viability decreased drastically with an increase in the concentration of ICG-Lips. The viability of A375 cells decreased to 30% when the concentration of ICG-Lips was $80 \text{ }\mu\text{g/mL}$, which was selected for subsequent studies owing to the balance between bioavailability and efficacy. This concentration was also aligned with that chosen for PTT ([Figure S3B](#)).

After confirming the favorable targeting and action conditions of ICG-Lips combined with MMBs, the *in vitro* anticancer effects of ICG-Lips combined with MMBs were validated. The *in vitro* anti-melanoma performance of ICG-Lips in combination with MMBs was analyzed using calcein-AM and propidium iodide (PI) (live/dead) staining, Annexin V-FITC/PI apoptosis assay, and CCK-8 assay.²⁴ The grouping settings were the same as those for ROS ingestion detection, with a total of 15 groups. In CCK-8 assay ([Figure 4A](#)), A375 cell viability was above 90% in Groups 1, 2, 3, 4, 5, 6, 7, 10, and 13 groups, whereas A375 cell viability decreased to a range of 70%-15% in Groups 8, 9, 11, 12, 14, and 15 groups. Group 15 showed the most pronounced cytotoxicity. Such differences in cell viability may be due to the efficacy of PTT and differences in PDT induced by different ROS generated under different treatments ([Figure 3B and D](#)), resulting in different degrees of cytotoxicity. In live/dead cell quantification ([Figure 4B](#)) and staining ([Figure 4C](#)), minimal red signals were observed in groups 1, 2, 3, 4, 5, 6, 7, 10, and 13, while red fluorescence increased significantly to varying degrees in groups 9, 11, 12, 14, and 15. Among them, group 15 showed the strongest red signal. The results were consistent with those of the CCK-8 assay. Cell viability was further assessed using the Annexin V-FITC / PI staining assay ([Figure 4D and E](#)), revealing that the synergistic treatment in group 15 resulted in the highest level of cell death (85.4%) among all groups. Taken together, these findings indicated that ICG-Lips combined with MMBs significantly inhibited the growth of melanoma cells.

The Mechanism of ICG-Lips Combination with MMBs Anticancer Effects

We also explored the potential mechanism of ICG-Lips combined with MMBs in inhibiting melanoma cell growth. Ferroptosis, characterized by iron-dependent lipid peroxidation, has emerged as a focal point of investigation. Both mPTT and PDT can induce ferroptosis onset. PTAs produce free radicals after absorbing light energy during PTT, which can promote lipid peroxidation and thereby causing ferroptosis.⁶² In addition, owing to increased temperature, ferroptosis can be promoted via catalysis of the Fenton reaction.⁶³ mPTT can promote the release and accumulation of intracellular iron ions through local hyperthermia, increasing the occurrence of lipid peroxidation and thereby inducing ferroptosis. One study has shown that a synergistic strategy of mutually reinforcing mPTT and ferroptosis can be effective in the treatment of breast cancer.⁶⁴ PDT promotes lipid peroxidation through reactive oxygen species (ROS), which, in turn, can cause ferroptosis. For instance, under NIR excitation, ICG generates ROS, leading to ferroptosis in the fibrosarcoma cell line HT-1080.³² Based on these findings and the studies outlined above, it is reasonable to hypothesize that ferroptosis plays a crucial role in the anti-melanoma function of ICG-Lips combined with MMBs. Based on the results of the ROS assay, we set up eight groups to test the following hypotheses: 1- PBS (control); 2-free ICG + US + laser; 3-MMBs + US + laser; 4-ICG-Lips + US + laser; 5-ICG-Lips + MMBs + US; 6-ICG-Lips + MMBs + laser; 7-ICG-Lips + MMBs + US + laser (synergistic treatment group); and 8-ICG-Lips + MMBs + US + laser + Fer-1.

Subsequently, the intracellular GSH levels in the various treatments were examined, and it was found that free ICG led to a decline in intracellular GSH levels under ultrasound and laser excitation. The synergistic treatment group had significantly lower GSH levels than the other groups ([Figure 5A](#)). Western blotting was used to examine the expression of GPX4, as this protein is affected by GSH levels and has been reported to be a biomarker of ferroptosis.⁶⁵ When GPX4 is dysfunctional, lipids are converted to lipid ROS, along with oxygen (O_2) and ferrous ions (Fe^{2+}), leading to the

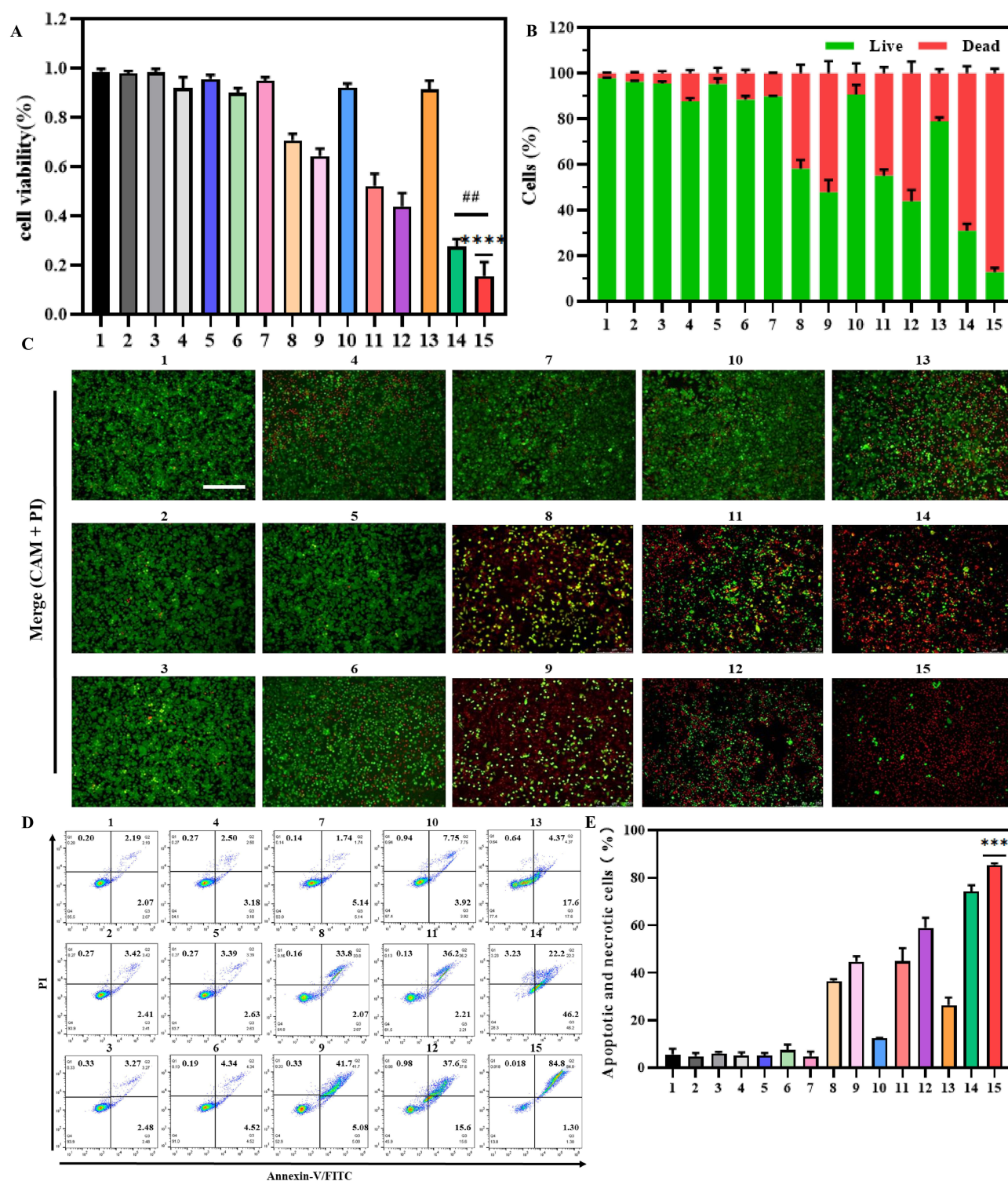


Figure 4 (A) CCK-8 cell viability assay for detecting cytotoxicity of various treatments towards A375 cells. (B) Quantitative results of (C). (C) Calcein AM/PI double stain (green: live cells; red: dead cells) of A375 cells after different treatments. Scale bar: 400 μ m. (D) Annexin V-FITC/PI apoptosis assay of A375 cells after various treatments. (E) Percentage of apoptotic and necrotic cells in Annexin V-FITC/PI apoptosis assay. US (1.5 W/cm², 20%, 1min); laser (808 nm, 2.0 W/cm², 10 min). The groups are set as: 1-US; 2-laser; 3-US + laser; 4-MMBs + US; 5-MMBs + laser; 6-MMBs + US + laser; 7-free ICG +US; 8-free ICG + laser; 9-free ICG +US + laser; 10-ICG-Lips + US; 11-ICG-Lips + laser; 12-ICG-Lips + US + laser; 13-ICG-Lips + MMBs + US; 14-ICG-Lips + MMBs + Laser, and 15-ICG-Lips + MMBs + US+ laser. n=3, ***p<0.001, ****p<0.0001, compared to the US group; ##p<0.01, compared to the ICG-Lips + MMBs + US + Laser group.

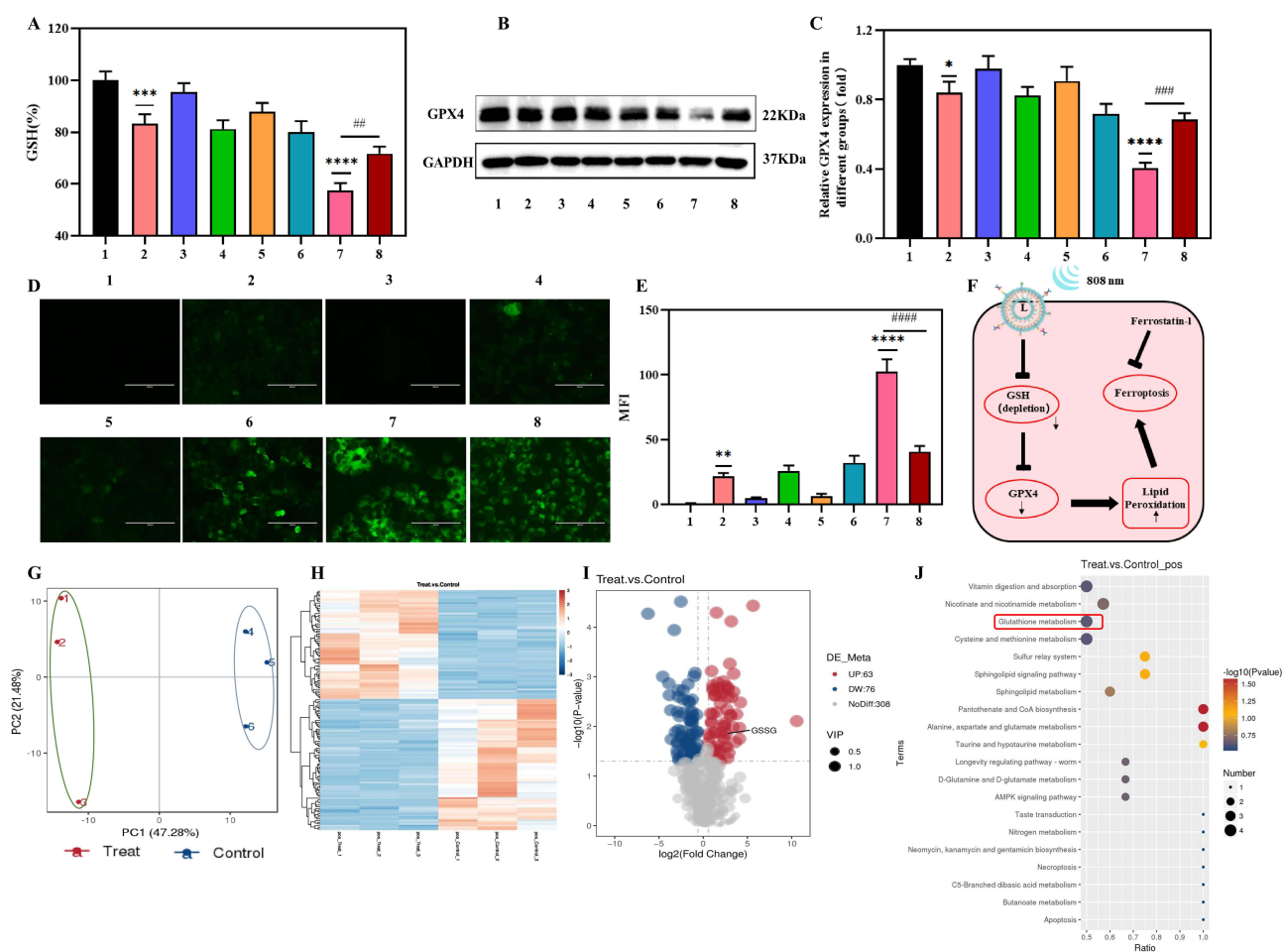


Figure 5 (A) GSH levels in A375 cells after different treatments. (B) Western blot analysis of GPX4 in A375 cells after different treatments. (C) The relative expression levels of GPX4 were calculated from (B). (D) Fluorescence images of lipid peroxides in BODIPY^{581/591}-C11 stained A375 cells after different treatments. Scale bar: 100 μ m. (E) The fluorescence intensity of lipid peroxides was calculated from (D). (F) The simplified mechanism of ferroptosis. (G) PCA score plot showing differences between the control and synergistic treatment group of A375 cells. (H) Heat map of metabolites in each treatment group. (I) Volcano plot demonstrating altered metabolite levels between the control and synergistic treatment groups. (J) Pathway analysis of significant differential metabolites between the control and synergistic treatment groups. Ion mode: positive. The groups are set as: 1- PBS (control); 2-free ICG + US + laser; 3-MMBs + US + laser; 4-ICG-Lips + US + laser; 5-ICG-Lips + MMBs + US; 6-ICG-Lips + MMBs + laser; 7-ICG-Lips + MMBs + US + laser (synergistic treatment group); and 8-ICG-Lips + MMBs + US + laser + Fer-1. n=3, ****p<0.0001, compared to the US group; ###p<0.01, ####p<0.001, compared to the ICG-Lips + MMBs + US + Laser group.

accumulation of LPO, which attacks intracellular biomolecules and ultimately kills cells. As depicted in Figure 5B and C, our findings revealed a significant downregulation of GPX4 expression in the synergistic treatment group compared with the other groups. Additionally, LPO accumulation was the most pronounced in the synergistic treatment group (Figure 5D and E). The introduction of Fer-1, an effective and selective inhibitor of ferroptosis,⁶⁶ increased intracellular GSH levels and upregulated GPX4 expression compared with the synergistic treatment group. There was a simultaneous decrease in the production of LPO compared to that in the synergistic treatment group (Figure 5A-D), which further illustrated that ferroptosis plays an essential role in the treatment employing ICG-Lips in combination with MMBs.

Based on these results, it is reasonable to assume that the mechanism of ferroptosis in A375 cells induced by the synergistic treatment group may have consumed large amounts of intracellular GSH under 808 nm laser irradiation. This depletion of GSH led to GPX4 downregulation and lipid peroxidation (LPO) accumulation, resulting in heightened ferroptosis (Figure 5F). To further investigate this mechanism, we conducted untargeted metabolomic profiling of cells from the control and synergistic treatment groups, using ultra-performance liquid chromatography-tandem mass spectrometry (UPLC-MS/MS). As illustrated by the principal component analysis (PCA) scores (Figure 5G and Figure S7A), both groups exhibited clear separation trends in both positive and negative ion modes. Heatmaps of differential metabolites in the control and synergistic treatment groups are shown in Figure 5H and Figure S7B. Through metabolite

screening (fold change < 0.67 or ≥ 1.5 , $p < 0.05$), 327 metabolites were identified between the control and co-treatment groups, with 139 significantly different metabolites in the positive ion mode (Figure 5I and Table S2) and 188 differential metabolites in the negative ion mode (Figure S7C and Table S3).

Further KEGG enrichment analysis of the differential metabolites, visualized through a bubble chart, revealed that the metabolites altered in both positive and negative ion modes between the control and synergistic treatment groups were primarily associated with glutathione metabolism, glutamate, niacin, and nicotinamide metabolism (Figure 5J and Figure S7D). Notably, compared to the control group, the levels of GSSG, L-glutamic acid, and adenosine triphosphate (ATP) were significantly upregulated in the synergistic treatment group. L-Glutamic acid and ATP are key precursors of glutathione synthesis. GSSG accumulation is typically reduced to GSH by nicotinamide adenine dinucleotide phosphate (NADPH), a process that may lead to potential cellular toxicity. Additionally, previous reports have shown that glutamate, niacin, and nicotinamide metabolism is closely linked to reactive oxygen species (ROS) generation. Overall, the metabolomic data suggest that the synergistic treatment specifically disrupts glutathione metabolic processes, ultimately inducing ferroptosis in A375 cells.

In vivo Targeting Evaluation

Inspired by the results of the in vitro experiments, further in vivo experiments were conducted. To ascertain whether the as-fabricated ICG-Lips exhibited improved stability and targeting compared to free ICG in vivo, a tumor-bearing mouse model was initially established using melanoma cell A375. Subsequently, free ICG and ICG-Lips (5 mg/kg, ICG) were intravenously injected into tumor-bearing mice, and near-infrared imaging of free ICG and ICG-Lips was performed using a small animal in vivo imaging system.

As shown in Figure 6A and B, for the free ICG group, the fluorescence signals at the tumor site gradually decreased with time, whereas those of the ICG-Lips group gradually increased with time, reaching a peak at 12h, indicating that the ICG-Lips had excellent tumor accumulation ability. The favorable tumor accumulation ability of ICG-Lips is partly

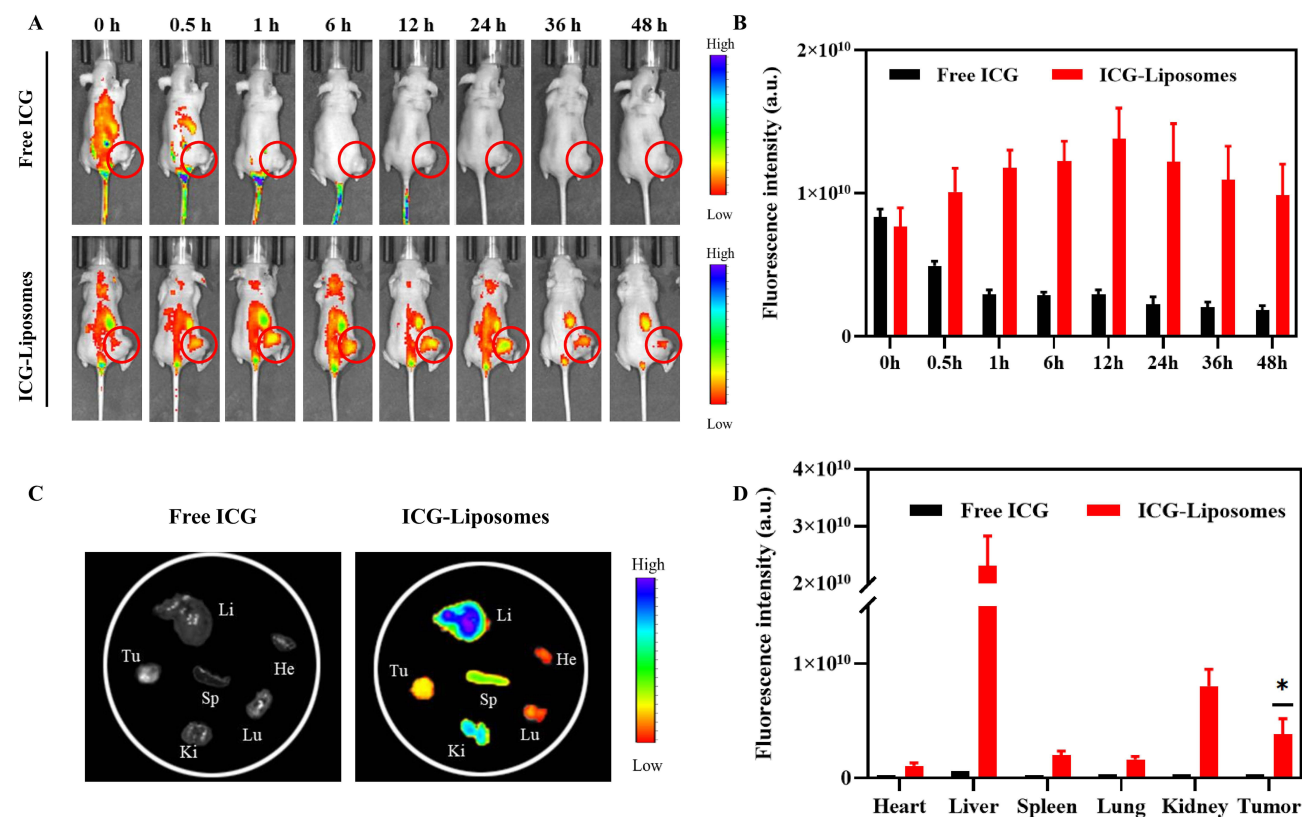


Figure 6 (A). In vivo fluorescence imaging of the mice at different time points after intravenous injection of free ICG and ICG-Lips. The red circles highlight the tumor locations of the mice. (B) quantitative results of (A). (C) Ex vivo biodistribution imaging of free ICG and ICG-Lips 48 h post-injection into tumor-bearing mice, (D) quantitative results of (C). $n=4$, * $p<0.05$, compared to the free ICG group.

attributed to well-known passive targeting, that is, enhanced penetration and retention effect (EPR), and partly to active targeting originating from the interaction of the S100B protein overexpressed in melanoma cells with the S100B-specific antibody of ICG-Lips. Moreover, the enhanced stability of ICG within liposomes in the surrounding environment, which prevents its binding to plasma proteins and thereby improves circulation time, could also account for the robust tumor accumulation capacity of ICG-Lips.⁶⁷ After NIR imaging, tumors and major organs were extracted from the mice injected with free ICG and ICG-Lips for ex vivo fluorescence imaging analysis (Figure 6C and D). The fluorescence intensity of ICG was weak at both tumor sites and major organs in mice injected with free ICG. The prominent ICG (ICG-Lips) fluorescence signals observed in the liver and kidney may be attributed to the liposome coating, which reduces the interception of ICG-Lips by the liver and kidney and to the liver as the main metabolic organ for ICG nanoparticles.^{67,68} Additionally, the prominent signals observed at the tumor site reaffirmed the promising tumor accumulation capacity of the ICG-Lips.

To confirm the in vivo targeting of MMBs, DIR-labeled MMBs were injected intravenously into mice bearing A375 tumors, and it was found that MMBs immediately aggregated at the tumor site after injection in the presence of an external magnet. After the removal of the external magnet, the fluorescence gradually diminished (Figure S8A). This phenomenon was attributed to the excellent magnetic responsiveness of MMBs, thus confirming that the synthesized MMBs exhibited robust targeting properties in vivo. At the end of 48 h of observation, major organs and tumors, such as the heart, liver, spleen, lungs, and kidneys, were extracted for the fluorescence assay, and no significant aggregation was observed in each organ or tumor site (Figure S8B), which might be the result of their metabolism in the liver, spleen, and lungs and was also consistent with our previous report.⁶⁹

Anticancer Effects in vivo

Inspired by the aforementioned results, the in vivo anti-tumor effects of synergistic treatment involving ICG-Lips combined with MMBs were investigated. Following grouping established in the mechanistic study section, mice bearing subcutaneous A375 tumors were randomly divided into eight groups with the same grouping settings as in the mechanism section. A schematic illustration of the synergistic treatment group is shown in Figure 7A. The treatment program for the other groups was accordingly adjusted. Over the following 14 days, the tumor volume and body weight of each group of mice were dynamically monitored and recorded to generate a tumor growth curve (Figure 7B). After the treatment period, all mice were euthanized and their tumors were excised, photographed, and weighed (Figure 7C and D) to evaluate their therapeutic efficacy. Compared to the control (1) group, there was no significant tumor inhibitory effect in groups 3 and 5, whereas groups 2, 4, 6, 7, and 8 demonstrated various levels of tumor inhibition. Among the various treatments, the synergistic treatment group demonstrated the most remarkable tumor inhibition, which can primarily be attributed to the multidimensional therapeutic effects of PTT and ferroptosis-enhanced PDT, as discussed above.

To further confirm the synergistic anti-tumor mechanism of the synergistic treatment group, hematoxylin and eosin (H&E) staining, Ki67 assay, TUNEL assay, and GPX4 immunohistochemical analyses were conducted at the end of the treatment to assess histological changes in the tumors (Figures 7E and S9). Consistent with the results of the aforementioned tumor growth assessment, the ability of the different treatment approaches to inhibit tumor growth varied. The H&E staining results of the synergistic treatment group showed the most pronounced tumor cell death, the lowest Ki67 positivity, the highest TUNEL positivity, and the most downregulated GPX4 expression, further confirming the superior therapeutic efficacy of the synergistic treatment of melanoma with ICG-Lips in combination with MMBs.

Finally, the potential systemic toxicity and biosafety of the different therapeutic approaches were examined, which are important for clinical applications. First, we monitored the body weights of the mice in each group throughout the treatment period and did not observe statistically significant differences in body weight. (Figure S10). Variation in the morphology and weight of the liver and kidney in all groups of mice was negligible (Figure S11A and B). Serum biochemical analyses revealed no remarkable differences in these biochemical indices between the groups (Figure S12), suggesting that no significant hepatic or renal toxicity was associated with the treatment strategy. Hematological analyses, including leukocyte, erythrocyte, hemoglobin, platelet, erythrocyte pressure volume, mean erythrocyte volume, mean erythrocyte hemoglobin, and mean erythrocyte hemoglobin, showed no significant differences between the groups (Figure S13), indicating that there was no obvious systemic toxicity associated with the treatment strategy. These data

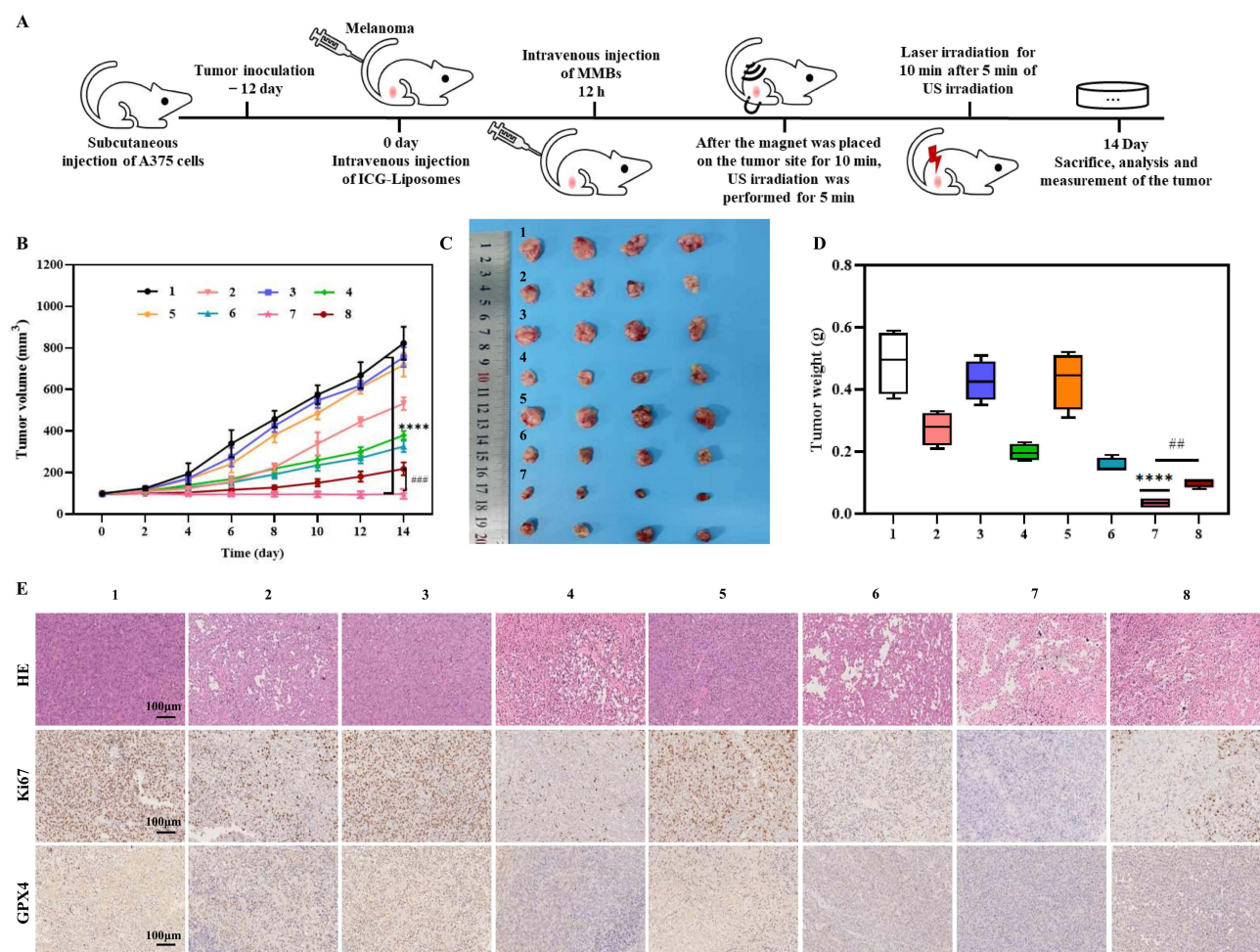


Figure 7 (A) In vivo treatment schedule of ICG-Lips in combination with MMBs. (B) Photographs of tumors in different treatment groups at the end of treatment. (C) The growth curves of mice A375 tumors after various treatments. (D) Tumor weights at the end of treatment for the different treatment groups. (E) H&E staining, Ki67, and GPX4 immunohistochemical staining of tumors from different groups at the end of treatment. US (1.5 W/cm², 20%, 5 min), laser (808 nm, 2 W/cm², 10 min). The groups are set as: 1- PBS (control); 2-free ICG + US + laser; 3-MMBs + US + laser; 4-ICG-Lips + US + laser; 5-ICG-Lips + MMBs + US; 6-ICG-Lips + MMBs + laser; 7-ICG-Lips + MMBs + US + laser (synergistic treatment group); and 8-ICG-Lips + MMBs + US + laser + Fer-I. n=4, ****p<0.0001, compared to the US group, ###p<0.01, ####p<0.001, compared to the ICG-Lips + MMBs + US + laser group. Scale bar: 100 μm.

illustrate that the synergistic treatments are biocompatible and acceptable. Furthermore, the major organs were harvested and histopathological changes in the major organs were assessed using H&E staining. No significant physiological abnormalities were observed in any of the groups, confirming the safety profile of the combined treatment involving ICG-lips and MMBs (Figure S14).

Conclusion

In conclusion, ICG-Lips and MMBs were synthesized using a convenient thin-film hydration method for synergistic treatment of melanoma through mPTT and ferroptosis-enhanced PDT. The synthesized MMBs demonstrated excellent responsiveness to magnetic fields and promoted rapid and efficient uptake of ICG-Lips by melanoma cells under US mediation. In addition, they augment ROS generation, thereby enhancing the efficacy of PDT. The synthesized ICG-Lips exhibited favorable stability and tumor-targeting ability. Under 808 nm laser irradiation, ICG-Lips entering melanoma cells increased the temperature, leading to superior mPTT, abundant ROS generation for enhanced PDT efficacy, disruption of the redox balance, and consumption of considerable amounts of GSH to initiate ferroptosis. Disruption of the redox balance caused by ferroptosis leads to an increase in the concentration of oxidants, further enhancing the efficacy of PDT. At both the cellular and tumor-bearing animal levels, a therapeutic approach involving ICG-Lips

combined with MMBs achieved notable inhibition of melanoma cells and tumor growth. Furthermore, this therapeutic strategy resulted in minimal effects on major healthy organs, blood counts, blood biochemistry, liver function, and kidney function. Therefore, the combination of ICG-Lips with MMBs achieved the integration of mPTT and ferroptosis-enhanced PDT, thereby enhancing anticancer efficacy. This approach offers a novel, biocompatible, safe, and effective therapeutic option for the treatment of melanoma.

Data Sharing Statement

All data generated or analyzed during this study are included in this article and its [supplementary information documents](#).

Funding

This work is supported by the Shenzhen Medical Research Fund (A2302009), SanmingProject of Medicine in Shenzhen (No. SZSM202211025), the National Natural Science Foundation of China (Grant Nos. 82073019 and 82073018), and Shenzhen Science and Technology Innovation Commission, China (Natural Science Foundation of Shenzhen, JCYJ20210324114212035).

Disclosure

The authors declare that the concepts and information presented in this paper are based on research and not commercially available. The authors declare that they have no conflict of interest.

References

1. Siegel RL, Giaquinto AN, Jemal A. Cancer statistics, 2024, CA. *Cancer J Clin.* 2024;74(1):12–49. doi:10.3322/caac.21820
2. Sacchetto L, Rosso S, Comber H, et al. Skin melanoma deaths within 1 or 3 years from diagnosis in Europe. *Int. J. Cancer.* 2021;148:2898–2905. doi:10.1002/ijc.33479
3. Long GV, Swetter SM, Menzies AM, Gershenwald JE, Scolyer RA. Cutaneous melanoma. *Lancet Lond Engl.* 2023;402:485–502. doi:10.1016/S0140-6736(23)00821-8
4. Guo W, Wang H, Li C. Signal pathways of melanoma and targeted therapy. *Signal Transduct Target Ther.* 2021;6:424. doi:10.1038/s41392-021-00827-6
5. Chorti E, Kowall B, Hassel JC, et al. Association of antibiotic treatment with survival outcomes in treatment-naïve melanoma patients receiving immune checkpoint blockade. *Eur J Cancer Oxf Engl.* 2024;200:113536. doi:10.1016/j.ejca.2024.113536
6. Wang L, Tang Y. N6-methyladenosine (m6A) in cancer stem cell: from molecular mechanisms to therapeutic implications, Biomed. *Pharmacother Biomedecine Pharmacother.* 2023;163:114846. doi:10.1016/j.biopha.2023.114846
7. Butrovich MA, Qin J, Xue X, Ivy SP, Nolin TD, Beumer JH. Impact of the 2021 CKD-EPI equation on anticancer pharmacotherapy in black and non-black cancer patients. *Cancer Lett.* 2024;586:216679. doi:10.1016/j.canlet.2024.216679
8. Liu S, Tian H, Ming H, et al. Mitochondrial-Targeted CS@KET/P780 nanoplatfor for site-specific delivery and high-efficiency cancer immunotherapy in hepatocellular carcinoma. *Adv Sci Weinh Baden-Wurt Ger.* 2024;11:e2308027. doi:10.1002/advs.202308027
9. Barenholz Y. Doxil®—the first FDA-approved nano-drug: lessons learned. *J Control Release off J Control Release Soc.* 2012;160:117–134. doi:10.1016/j.jconrel.2012.03.020
10. Tang J-Q, Hou X-Y, Yang C-S, et al. Recent developments in nanomedicine for melanoma treatment. *Int J Cancer.* 2017;141:646–653. doi:10.1002/ijc.30708
11. Zeng H, Li J, Hou K, Wu Y, Chen H, Ning Z. Melanoma and nanotechnology-based treatment. *Front Oncol.* 2022;12:858185. doi:10.3389/fonc.2022.858185
12. Yang H, Xu B, Li S, et al. A photoresponsive nanozyme for synergistic catalytic therapy and dual phototherapy, small weinh. *Bergstr Ger.* 2021;17:e2007090. doi:10.1002/sml.202007090
13. Sun Q, Li Y, Shen W, et al. Breaking-down tumoral physical barrier by remotely unwrapping metal-polyphenol-packaged hyaluronidase for optimizing photothermal/photodynamic therapy-induced immune response. *Adv Mater Deerfield Beach Fla.* 2024;36(18):e2310673. doi:10.1002/adma.202310673
14. Liu Y, Bhattarai P, Dai Z, Chen X. Photothermal therapy and photoacoustic imaging via nanotheranostics in fighting cancer. *Chem Soc Rev.* 2019;48(7):2053–2108. doi:10.1039/c8cs00618k
15. Chu KF, Dupuy DE. Thermal ablation of tumours: biological mechanisms and advances in therapy. *Nat Rev Cancer.* 2014;14(3):199–208. doi:10.1038/nrc3672
16. Evans SS, Repasky EA, Fisher DT. Fever and the thermal regulation of immunity: the immune system feels the heat. *Nat Rev Immunol.* 2015;15(6):335–349. doi:10.1038/nri3843
17. Pandesh S, Haghooy Javanmard S, Shakeri-Zadeh A, Shokrani P. Targeted photothermal therapy of melanoma in C57BL/6 Mice using Fe3O4@Au core-shell nanoparticles and near-infrared laser. *J Biomed Phys Eng.* 2021;11(1):29–38. doi:10.31661/jbpe.v0i0.736
18. Vilas-Boas V, Carvalho F, Espiña B. Magnetic hyperthermia for cancer treatment: main parameters affecting the outcome of in vitro and in vivo studies. *Mol Basel Switz.* 2020;25:2874. doi:10.3390/molecules25122874
19. Gao G, Jiang Y-W, Guo Y, et al. Enzyme-mediated tumor starvation and phototherapy enhance mild-temperature photothermal therapy. *Adv Funct Mater.* 2020;30(16):1909391. doi:10.1002/adfm.201909391

20. Jiang Z, Li T, Cheng H, et al. Nanomedicine potentiates mild photothermal therapy for tumor ablation. *Asian J Pharm Sci.* **2021**;16(6):738–761. doi:10.1016/j.ajps.2021.10.001
21. Wang N, Zhao Z, Xiao X, et al. ROS-responsive self-activatable photosensitizing agent for photodynamic-immunotherapy of cancer. *Acta Biomater.* **2023**;164:511–521. doi:10.1016/j.actbio.2023.03.038
22. Xie J, Wang Y, Choi W, et al. Overcoming barriers in photodynamic therapy harnessing nano-formulation strategies. *Chem Soc Rev.* **2021**;50(16):9152–9201. doi:10.1039/d0cs01370f
23. Lucena SR, Salazar N, Gracia-Cazaña T, et al. Combined treatments with photodynamic therapy for non-melanoma skin cancer. *Int J mol Sci.* **2015**;16(10):25912–25933. doi:10.3390/ijms161025912
24. Wang X, Wu M, Zhang X, et al. Hypoxia-responsive nanoreactors based on self-enhanced photodynamic sensitization and triggered ferroptosis for cancer synergistic therapy. *J Nanobiotechnology.* **2021**;19(1):204. doi:10.1186/s12951-021-00952-y
25. Wang H, Zhang C, Zhang Y, et al. An efficient delivery of photosensitizers and hypoxic prodrugs for a tumor combination therapy by membrane camouflage nanoparticles. *J Mater Chem B.* **2020**;8(14):2876–2886. doi:10.1039/d0tb00235f
26. Xiao X, Chen M, Zhang Y, et al. Hemin-incorporating DNA nanozyme enabling catalytic oxygenation and GSH depletion for enhanced photodynamic therapy and synergistic tumor ferroptosis. *J Nanobiotechnology.* **2022**;20(1):410. doi:10.1186/s12951-022-01617-0
27. Hu X, Li J, Chen Y, et al. A self-assembly ICG nanoparticle potentiating targeted photothermal and photodynamic therapy in NSCLC. *ACS Biomater Sci Eng.* **2022**;8(10):4535–4546. doi:10.1021/acsbomaterials.2c00620
28. Wang D, Yue J, Cao Q, et al. ICG-loaded and 125I-labeled theranostic nanosystem for multimodality imaging-navigated phototherapy of breast cancer. *Biomater Sci.* **2022**;11(1):248–262. doi:10.1039/d2bm01551j
29. Li S, Yang S, Liu C, et al. Enhanced photothermal-photodynamic therapy by indocyanine green and curcumin-loaded layered MoS₂ hollow spheres via inhibition of P-Glycoprotein. *Int J Nanomed.* **2021**;16:433–442. doi:10.2147/IJN.S275938
30. Ledezma DK, Balakrishnan PB, Cano-Mejia J, et al. Indocyanine green-nexturastat A-PLGA nanoparticles combine photothermal and epigenetic therapy for melanoma. *Nanomater Basel Switz.* **2020**;10(1):161. doi:10.3390/nano10010161
31. Chen Z, Huang Q, Song Y, et al. Cubosomes-assisted transdermal delivery of doxorubicin and indocyanine green for chemo-photothermal combination therapy of melanoma. *Biomed Pharmacother Biomedecine Pharmacother.* **2023**;166:115316. doi:10.1016/j.biopha.2023.115316
32. Tseng H-C, Kuo C-Y, Liao W-T, Chou T-S, Hsiao J-K. Indocyanine green as a near-infrared theranostic agent for ferroptosis and apoptosis-based, photothermal, and photodynamic cancer therapy. *Front Mol Biosci.* **2022**;9:1045885. doi:10.3389/fmolb.2022.1045885
33. Castañeda-Reyes ED, de J. Perea-Flores M, Davila-Ortiz G, Lee Y, Gonzalez de Mejia E. Development, characterization and use of liposomes as amphipathic transporters of bioactive compounds for melanoma treatment and reduction of skin inflammation: a review. *Int J Nanomed.* **2020**;15:7627–7650. doi:10.2147/IJN.S263516
34. Tenchov R, Bird R, Curtze AE, Zhou Q. Lipid nanoparticles—from liposomes to mRNA vaccine delivery, a landscape of research diversity and advancement. *ACS Nano.* **2021**;15(11):16982–17015. doi:10.1021/acsnano.1c04996
35. Jang KW, Seol D, Ding L, Lim T-H, Frank JA, Martin JA. Ultrasound-mediated microbubble destruction suppresses melanoma tumor growth. *Ultrasound Med Biol.* **2018**;44(4):831–839. doi:10.1016/j.ultrasmedbio.2017.12.011
36. Zhu Y, Liu Y, Khan K, et al. Ultrasound combined with nanomaterials for cancer therapy. *Mater Today Adv.* **2023**;17:100330. doi:10.1016/j.mtadv.2022.100330
37. Lemaître S, Thaug C, Damato B. Extrascleral extension from choroidal melanoma diagnosed on Doppler ultrasound. *Ophthalmology.* **2022**;129:405. doi:10.1016/j.ophtha.2021.10.019
38. Kooiman K, Vos HJ, Versluis M, de Jong N. Acoustic behavior of microbubbles and implications for drug delivery. *Adv Drug Deliv Rev.* **2014**;72:28–48. doi:10.1016/j.addr.2014.03.003
39. Dimcevski G, Kotopoulos S, Bjånes T, et al. A human clinical trial using ultrasound and microbubbles to enhance gemcitabine treatment of inoperable pancreatic cancer. *J Control Release off J Control Release Soc.* **2016**;243:172–181. doi:10.1016/j.jconrel.2016.10.007
40. Liu Z, Lammers T, Ehling J, et al. Iron oxide nanoparticle-containing microbubble composites as contrast agents for MR and ultrasound dual-modality imaging. *Biomaterials.* **2011**;32(26):6155–6163. doi:10.1016/j.biomaterials.2011.05.019
41. Fan C-H, Cheng Y-H, Ting C-Y, et al. Ultrasound/Magnetic Targeting with SPIO-DOX-microbubble complex for image-guided drug delivery in brain tumors. *Theranostics.* **2016**;6(10):1542–1556. doi:10.7150/thno.15297
42. Ikeda-Imafuku M, Wang LL-W, Rodrigues D, Shaha S, Zhao Z, Mitragotri S. Strategies to improve the EPR effect: a mechanistic perspective and clinical translation. *J Control Release off J Control Release Soc.* **2022**;345:512–536. doi:10.1016/j.jconrel.2022.03.043
43. Yi H, Lu W, Liu F, et al. ROS-responsive liposomes with NIR light-triggered doxorubicin release for combinatorial therapy of breast cancer. *J Nanobiotechnology.* **2021**;19(1):134. doi:10.1186/s12951-021-00877-6
44. Gao D, Luo Z, He Y, et al. Low-dose NIR-II preclinical bioimaging using liposome-encapsulated cyanine dyes. *Small Weinb Bergstr Ger.* **2023**;19(17):e2206544. doi:10.1002/smll.202206544
45. Liu P, Lan S, Gao D, et al. Targeted blood-brain barrier penetration and precise imaging of infiltrative glioblastoma margins using hybrid cell membrane-coated ICG liposomes. *J Nanobiotechnology.* **2024**;22(1):603. doi:10.1186/s12951-024-02870-1
46. Loading of indocyanine green within polydopamine-coated laponite nanodisks for targeted cancer photothermal and photodynamic therapy - pubMed, (n.d.). Available from: <https://pubmed.ncbi.nlm.nih.gov/29783745/>. (Accessed January 25, 2025.).
47. Lee E-H, Lee M-K, Lim S-J. Enhanced stability of indocyanine green by encapsulation in zein-phosphatidylcholine hybrid nanoparticles for use in the phototherapy of cancer. *Pharmaceutics.* **2021**;13(3):305. doi:10.3390/pharmaceutics13030305
48. Zhang L, Song X, Qi Q, Liu W. Interaction of DPPC liposomes with cholesterol and food protein during *in vitro* digestion using Dynamic Light Scattering and FTIR spectroscopy analysis. *Food Chem.* **2022**;375:131893. doi:10.1016/j.foodchem.2021.131893
49. Baird G, Farrell C, Cheung J, Sempale A, Blue J, Ahl PL. FTIR spectroscopy detects intermolecular β -sheet formation above the high temperature T_m for two monoclonal antibodies. *Protein J.* **2020**;39(4):318–327. doi:10.1007/s10930-020-09907-y
50. Derenne A, Derfoufi K-M, Cowper B, Delporte C, Goormaghtigh E. FTIR spectroscopy as an analytical tool to compare glycosylation in therapeutic monoclonal antibodies. *Anal Chim Acta.* **2020**;1112:62–71. doi:10.1016/j.aca.2020.03.038
51. An F, Yang Z, Zheng M, et al. Rationally assembled albumin/indocyanine green nanocomplex for enhanced tumor imaging to guide photothermal therapy. *J Nanobiotechnology.* **2020**;18(1):49. doi:10.1186/s12951-020-00603-8

52. Magnetic black phosphorus microbubbles for targeted tumor theranostics, (n.d.). Available from: <https://www.degruyter.com/document/doi/10.1515/nanoph-2021-0085/html>. (Accessed January 21, 2025).
53. Liu Y, Lai X, Zhu Y, et al. Contrast-enhanced ultrasound imaging using long-circulating cationic magnetic microbubbles in vitro and in vivo validations. *Int J Pharm.* **2022**;616:121299. doi:10.1016/j.ijpharm.2021.121299
54. Lin X, Wu M, Li M, et al. Photo-responsive hollow silica nanoparticles for light-triggered genetic and photodynamic synergistic therapy. *Acta Biomater.* **2018**;76:178–192. doi:10.1016/j.actbio.2018.07.007
55. Jin X, Lu X, Zhang Z, Lv H. Indocyanine green-parthenolide thermosensitive liposome combination treatment for triple-negative breast cancer. *Int J Nanomed.* **2020**;15:3193–3206. doi:10.2147/IJN.S245289
56. Sun X, Ye Q, Liang Y, et al. Chiral cysteine-copper ion-based assemblies for improved phototherapy. *J Colloid Interface Sci.* **2024**;657:993–1002. doi:10.1016/j.jcis.2023.11.170
57. Xie T, Qi Y, Li Y, et al. Ultrasmall Ga-ICG nanoparticles based gallium ion/photodynamic synergistic therapy to eradicate biofilms and against drug-resistant bacterial liver abscess. *Bioact Mater.* **2021**;6(11):3812–3823. doi:10.1016/j.bioactmat.2021.03.032
58. Lai Y, Lu N, Ouyang A, Zhang Q, Zhang P. Ferroptosis promotes sonodynamic therapy: a platinum(ii)-indocyanine sonosensitizer. *Chem Sci.* **2022**;13(34):9921–9926. doi:10.1039/d2sc02597c
59. Omata D, Unga J, Suzuki R, Maruyama K. Lipid-based microbubbles and ultrasound for therapeutic application. *Adv Drug Deliv Rev.* **2020**;154:–155:236–244. doi:10.1016/j.addr.2020.07.005
60. Sheng Z, Hu D, Zheng M, et al. Smart human serum albumin-indocyanine green nanoparticles generated by programmed assembly for dual-modal imaging-guided cancer synergistic phototherapy. *ACS Nano.* **2014**;8(12):12310–12322. doi:10.1021/nn5062386
61. Ghanem G, Loir B, Morandini R, et al. EORTC melanoma group, on the release and half-life of S100B protein in the peripheral blood of melanoma patients. *Int. J. Cancer.* **2001**;94(4):586–590. doi:10.1002/ijc.1504
62. Xie L, Li J, Wang G, et al. Phototheranostic metal-phenolic networks with antiexosomal PD-L1 enhanced ferroptosis for synergistic immunotherapy. *J Am Chem Soc.* **2022**;144(2):787–797. doi:10.1021/jacs.1c09753
63. Cui X, Lu G, Fang F, et al. Iron self-boosting polymer nanoenzyme for low-temperature photothermal-enhanced ferrotherapy. *ACS Appl Mater Interfaces.* **2021**;13(26):30274–30283. doi:10.1021/acsami.1c01658
64. Liu Z, Liu S, Liu B, et al. Facile synthesis of Fe-based metal-quinone networks for mutually enhanced mild photothermal therapy and ferroptosis. *Angew Chem Int Ed Engl.* **2025**;64(2):e202414879. doi:10.1002/anie.202414879
65. Liu Y, Wan Y, Jiang Y, Zhang L, Cheng W. GPX4: the hub of lipid oxidation, ferroptosis, disease and treatment. *Biochim Biophys Acta Rev Cancer.* **2023**;1878(3):188890. doi:10.1016/j.bbcan.2023.188890
66. Miotto G, Rossetto M, Di Paolo ML, et al. Insight into the mechanism of ferroptosis inhibition by ferrostatin-1. *Redox Biol.* **2020**;28:101328. doi:10.1016/j.redox.2019.101328
67. Egloff-Juras C, Bezdtnaya L, Dolivet G, Lassalle H-P. NIR fluorescence-guided tumor surgery: new strategies for the use of indocyanine green. *Int J Nanomed.* **2019**;14:7823–7838. doi:10.2147/IJN.S207486
68. Ngo W, Ahmed S, Blackadar C, et al. Why nanoparticles prefer liver macrophage cell uptake in vivo. *Adv Drug Deliv Rev.* **2022**;185:114238. doi:10.1016/j.addr.2022.114238
69. Zhu Y, Arkin G, Zeng W, et al. Ultrasound image-guided cancer gene therapy using iRGD dual-targeted magnetic cationic microbubbles. *Biomed Pharmacother Biomedecine Pharmacother.* **2024**;172:116221. doi:10.1016/j.biopha.2024.116221

International Journal of Nanomedicine

Publish your work in this journal

The International Journal of Nanomedicine is an international, peer-reviewed journal focusing on the application of nanotechnology in diagnostics, therapeutics, and drug delivery systems throughout the biomedical field. This journal is indexed on PubMed Central, MedLine, CAS, SciSearch®, Current Contents®/Clinical Medicine, Journal Citation Reports/Science Edition, EMBase, Scopus and the Elsevier Bibliographic databases. The manuscript management system is completely online and includes a very quick and fair peer-review system, which is all easy to use. Visit <http://www.dovepress.com/testimonials.php> to read real quotes from published authors.

Submit your manuscript here: <https://www.dovepress.com/international-journal-of-nanomedicine-journal>

Dovepress
Taylor & Francis Group